

GEOMETRY OF THE LARGE MAGELLANIC CLOUD DISK: RESULTS FROM MACHO AND THE TWO MICRON ALL SKY SURVEY

S. NIKOLAEV, A. J. DRAKE, S. C. KELLER, AND K. H. COOK

Institute for Geophysics and Planetary Physics, Lawrence Livermore National Laboratory, P.O. Box 808, L-413, Livermore, CA 94550; nikolaev2@llnl.gov

N. DALAL¹

Institute for Advanced Study, Princeton, NJ 08450; neal@ias.edu

K. GRIEST

Department of Physics, University of California at San Diego, Code 0354, 9500 Gilman Drive, La Jolla, CA 92093; griest@astrophys.ucsd.edu

D. L. WELCH

McMaster University, Hamilton, ON L8S 4M1, Canada; welch@physics.mcmaster.ca

AND

S. M. KANBUR

University of Massachusetts, Amherst, MA 01003; shashi@fcrao1.astro.umass.edu

Received 2003 June 27; accepted 2003 October 2

ABSTRACT

We present a detailed study of the viewing angles and geometry of the inner LMC ($\rho \lesssim 4^\circ$) based on a sample of more than 2000 MACHO Cepheids with complete $\{VR\}_{KC}$ light curves and single-phase Two Micron All Sky Survey (2MASS) JHK_s observations. The sample is considerably larger than any previously studied subset of LMC Cepheids and has an improved areal coverage. Single-epoch random-phase 2MASS photometry is corrected using MACHO V light curves to derive mean JHK_s magnitudes. We analyze the resulting period-luminosity relations in $VRJHK_s$ to recover statistical reddening and distance to each individual Cepheid, with respect to the mean distance modulus and reddening of the LMC. By fitting a plane solution to the derived individual distance moduli, the values of LMC viewing angles are obtained: position angle $\theta = 151^\circ 0 \pm 2^\circ 4$, inclination $i = 30^\circ 7 \pm 1^\circ 1$. In the so-called ring analysis, we find a strong dependence of the derived viewing angles on the adopted center of the LMC, which we interpret as being due to deviations from planar geometry. Analysis of residuals from the plane fit indicates the presence of a symmetric warp in the LMC disk and the bar elevated above the disk plane. Nonplanar geometry of the inner LMC explains a broad range for values of i and θ in the literature and suggests caution when deriving viewing angles from inner LMC data.

Subject headings: Cepheids — dust, extinction — galaxies: individual (Large Magellanic Cloud) — galaxies: structure

1. INTRODUCTION

At present, the issue of LMC geometry has several major implications concerning (1) the nature of the lensing population toward the LMC, (2) the dynamical state and evolution of the Milky Way–Magellanic Cloud system, and (3) possible systematic effect of the LMC inclination, coupled with in-plane age-metallicity gradients, on the extragalactic distance scale. Until recently, work in the field has been affected by small samples of standard candles and/or limited spatial coverage. In the last few years, a wealth of new data have become available from various surveys, enabling a truly global, multiband look at the LMC. Time domain data from microlensing surveys MACHO (Alcock et al. 2000) and OGLE (Udalski et al. 1992) are a valuable resource for stellar variability studies. The multiband data from several recent photometric surveys (Zaritsky, Harris, & Thompson 1997; Massey 2002; Goehrmann, Schmidt-Kaler, & Oestreicher 1992) are well suited to studying interstellar reddening and stellar populations. The data from two recent near-infrared (NIR) surveys, the Two Micron All Sky Survey (2MASS; Skrutskie 1998) and DENIS (Epchtein 1998), have the benefit of complete LMC coverage and low reddening.

On the modeling side, the viewing angles of the LMC derived from various photometric and kinematic tracers have been in rough agreement (Westerlund 1997): $\sim 170^\circ$ – 190° (counted east of north) for position angle of the line of nodes and $\sim 25^\circ$ – 45° for inclination, with the northeast quadrant being the closest. Recent determinations based on red clump magnitudes (Olsen & Salyk 2002) and Cepheids (Caldwell & Coulson 1986; Laney & Stobie 1986) gave somewhat lower position angles, $\theta \sim 145^\circ$. In their recent study based on carbon stars detected by 2MASS and DENIS, van der Marel & Cioni (2001, hereafter MC01) claimed a rather different position angle, $122^\circ 5 \pm 8^\circ 3$, by relaxing the condition of circular symmetry for the LMC disk. Such a drastically different position angle results in the LMC disk being strongly elliptical, $\epsilon = 0.31$ (van der Marel 2001). A similar result, $\theta = 129^\circ 9 \pm 6^\circ 0$, is derived by van der Marel et al. (2002) from kinematics of carbon stars in the outer LMC. In this paper we reexamine the viewing angles of the LMC, taking advantage of a large sample of MACHO Cepheids with available 2MASS photometry.

2. DATA AND SELECTION PROCEDURE

For this work, we have selected LMC Cepheids from MACHO complete 8 yr archive data. The stars were identified

¹ Hubble Fellow.

as Cepheids by MACHO light-curve analysis software. Preliminary classification of fundamental/overtone pulsation mode was obtained by a decision tree algorithm, based on a variety of numeric light-curve attributes. Our initial data set consisted of 3126 stars, which included 1966 fundamental-mode and 1160 first-overtone Cepheids (hereafter FU and FO, respectively). For each Cepheid, MACHO archival data included complete light curves in Kron-Cousins V and R , as well as a period estimate with typical accuracy of $\sigma_P/P \lesssim 10^{-4}$.

MACHO Cepheids were positionally matched to sources from the 2MASS All-Sky Release Catalog.² Coordinate matching was done using $3''$ radius. The sky distribution of matched Cepheids is displayed in Figure 1. All MACHO Cepheids are confined to the inner few degrees of the LMC, with no significant difference in distribution between FU and FO Cepheids. The figure shows higher surface density in the bar and northwest spiral arm, consistent with a young population. The geometric center of our sample is located at $\alpha \approx 80^\circ.4$, $\delta \approx -69^\circ.0$, with the majority of Cepheids within $\sim 4^\circ$ of the center ($1^\circ = 0.8728$ kpc at 50 kpc).

As part of the selection process, matched stars were screened for multiple detections, present as a result of overlapping fields in both MACHO and 2MASS. In addition, all 2MASS artifacts, such as diffraction spikes, persistence artifacts, glints, blends, etc., were removed. The issue of blending had to be addressed with some care, since the 2MASS image-processing pipeline does not actively deblend sources, meaning that stars with a bad point-spread function (PSF) fit are not split into multiple sources. Rather, the 2MASS blend flag is set when there is a detection within a certain distance of a source, typically $3''.5-4''$. Therefore, removing 2MASS “blends” does not guarantee that NIR magnitudes of our sample Cepheids are unaffected by flux from unresolved sources. To remove unresolved 2MASS blends, we used MACHO images to search for red stars, sufficiently bright and located close to our Cepheids. Using MACHO templates is justified, since the MACHO median template seeing of $1''.5$ is significantly better than the typical 2MASS FWHM of $2''-3''$. The brightness of a companion was made a function of distance, to reflect the change in proportion of mixed flux. Specifically, we checked the following conditions:

$$\begin{aligned} \Delta &< 3''.5, \\ R_b - R_{\text{Ceph}} &< \min\{2.0, 3.5 - 0.9\Delta\}, \\ (V - R)_b &> (V - R)_{\text{Ceph}}, \end{aligned} \quad (1)$$

where subscript “ b ” denotes a blend candidate and Δ is the angular separation between a blend and a Cepheid. If all the conditions given by equation (1) were met, the star was declared a blend and removed from our sample. Naturally, this procedure cannot remove Cepheids that are blended in MACHO images. Our outlier analysis in § 4.1 shows that only a small fraction (1.5%) of our Cepheids are significantly affected by blending with unresolved MACHO stars.

After finding the 2MASS counterparts and cleaning the sample, we proceeded to obtain Fourier series for MACHO light curves. Each light curve was fitted by an eighth-order Fourier series, taking into account photometric errors for each data point. After obtaining the fits, we visually inspected every light curve and its fitting series and rejected stars with poor fits or noisy light curves. In some cases, we have changed the

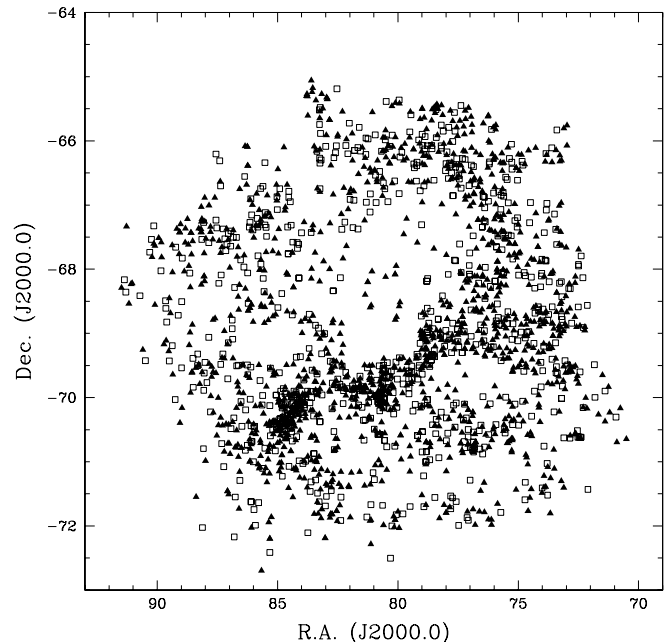


FIG. 1.—Sky distribution of sample Cepheids. Only MACHO Cepheids with 2MASS counterparts are plotted. Filled triangles denote FU Cepheids, while open squares denote FO Cepheids. Both distributions are consistent with a young population.

classification of Cepheid from FU to FO, or vice versa. In the classification decision for each Cepheid, the most weight was allocated to the position of the Cepheid in “ $R_{21} - \log P$ ” and “ $\phi_{21} - \log P$ ” diagrams. In cases in which these two tools were ambiguous, the decision was reached based on the position of the Cepheid in the combined “period-luminosity” (PL) diagram for five photometric bands ($VRJHK$). If this also failed to classify the Cepheid, it was removed from our sample.

As a result of our selection procedure, we obtained a sample of 2106 Cepheids (1357 FU and 749 FO). Most of the removed sources are 2MASS artifacts (46%), with smaller contributions due to blends (25%), stars that did not have a 2MASS counterpart within $3''$ (19%), and hard-to-classify Cepheids or poor light curve fits (10%). For each remaining Cepheid, available data include position, period, complete light curves in V and R , and a single measurement of JHK_s magnitudes from 2MASS.

2.1. Photometric Calibration

The photometric calibration procedure for MACHO data is described in Alcock et al. (1999). Photometry is calibrated to the standard Kron-Cousins V and R system. The internal (instrumental) accuracy of MACHO photometry is 0.019 in R and 0.021 in V . The systematic error is a function of location in the LMC: for the “top 30” MACHO fields the error is estimated to be 0.035 mag (for stars in the range $-0.1 \text{ mag} < V - R < 1.2 \text{ mag}$) and can be as large as 0.10 mag in the outer fields. When fitting MACHO light-curve shape with Fourier series, the only errors that matter are the random ones, since systematic error shifts the entire light curve up or down, without changing its shape. However, the mean magnitude derived from the fit must include the systematic error. We added the systematic errors (0.035 for top 30 fields, 0.10 for outer fields) in quadrature to the random errors for mean magnitudes derived from Fourier fit.

² See <http://irsa.ipac.caltech.edu>.

The single-phase 2MASS photometry is calibrated to the 2MASS internal photometric system, as described in Nikolaev et al. (2000). In principle, one has the option of converting the 2MASS photometry to the homogenized system of Bessell & Brett (1988) through color transformations provided by Carpenter (2001):

$$\begin{aligned} K_{2\text{MASS}} &= (0.000 \pm 0.005)(J - K)_{\text{BB}} - (0.044 \pm 0.003) + K_{\text{BB}}, \\ (J - H)_{2\text{MASS}} &= (0.980 \pm 0.009)(J - H)_{\text{BB}} - (0.045 \pm 0.006), \\ (J - K)_{2\text{MASS}} &= (0.972 \pm 0.006)(J - K)_{\text{BB}} - (0.011 \pm 0.005). \end{aligned} \quad (2)$$

The transformation to the Bessell & Brett (1988) system would simplify the treatment of interstellar reddening, since the response to the standard reddening law is well studied for the homogenized system. On the other hand, using the transformations given by equation (2) results in large statistical errors for NIR magnitudes, which carry over to distance errors. In fact, the analysis of residuals from a disk solution in this case suggests that these errors are overestimated, which is not surprising given that the color transformations in Carpenter (2001) were derived from preliminary 2MASS Second Incremental Release using a very limited sample of common stars. The analysis described below was carried out twice, using NIR magnitudes in the 2MASS internal system and in the homogenized system of Bessell & Brett (1988). The results for both cases were very similar, albeit more noisy for the homogenized system as a result of extra magnitude error from color transformations. Because of this, the results presented below are for NIR magnitudes in the 2MASS system.

3. METHOD

3.1. General Procedure

At the basis of all Cepheid distance determinations lies a PL relation,

$$\overline{M}_\lambda = \alpha_\lambda \log P + \beta_\lambda + \varepsilon_\lambda(M, T_e, Z, \dots). \quad (3)$$

Here λ denotes photometric band, $\lambda = \{V, R, J, H, K_s\}$, and $\varepsilon(\cdot)$ is some unknown function of stellar parameters, such as pulsation mass, effective temperature, metallicity, etc. The function $\varepsilon(\cdot)$ may also include correction terms due to non-linearity of the PL relation. Equation (3) is exact, as function $\varepsilon(\cdot)$ includes all parameters that affect the star's luminosity. Converting the mean intrinsic magnitude \overline{M}_λ to observed mean magnitude, we write the observed PL relation,

$$\begin{aligned} \overline{m}_\lambda &= \alpha_\lambda \log P + \beta_\lambda + \mu + R_\lambda E(B - V) \\ &+ \varepsilon_\lambda(M, T, Z, \dots). \end{aligned} \quad (4)$$

Here we parameterized the interstellar extinction in terms of the reddening vector \mathbf{R} whose components are ratios of the total to selective reddening, $R_\lambda = A_\lambda/E(B - V)$. For the homogenized Bessell & Brett (1988) photometric system, the reddening vector is

$$\begin{aligned} \mathbf{R} &= \{R_V, R_R, R_J, R_H, R_K\} \\ &= \{3.12, 2.56, 0.90, 0.53, 0.34\} \end{aligned} \quad (5)$$

(Bessell & Brett 1988; Taylor 1986). The reddening vector for the internal 2MASS photometric system is not available yet, but tests show that the results are not sensitive to the particular

choice of reddening vector: using other extinction laws, e.g., Cardelli, Clayton, & Mathis (1989), produces virtually identical results.

The system of equations given by equation (4) can be written for each Cepheid and contains five equations, one for each λ ($VRJHK_s$). Since the general form of the function ε_λ is unknown, we assume $\varepsilon_\lambda \in N(0, \sigma_{0,\lambda}^2)$, i.e., the main effect of the unknown physics is on the dispersion of the observed PL relation. Note that the dispersion is in general a function of wavelength. There is no loss of generality in assuming zero mean for the distribution of ε , since zero point β can always be shifted to accommodate any mean $\bar{\varepsilon}$. In equation (4), the distance modulus μ and reddening $E(B - V)$ can both be written as the sum of two parts, the mean quantity for the entire LMC and an offset that varies from star to star:

$$\begin{aligned} E(B - V)_i &= \overline{E(B - V)}_{\text{LMC}} + \Delta E(B - V)_i, \\ \mu_i &= \overline{\mu}_{\text{LMC}} + \Delta \mu_i. \end{aligned} \quad (6)$$

Here we introduced index i to denote individual stars. Substituting equation (6) in equation (4), we obtain

$$\overline{m}_{\lambda,i} = \alpha_\lambda \log P_i + \beta'_\lambda + \Delta \mu_i + R_\lambda \Delta E(B - V)_i, \quad (7)$$

where the average quantities $\overline{\mu}_{\text{LMC}}$ and $\overline{E(B - V)}_{\text{LMC}}$ have been incorporated into the new zero point β' . Given the observed $VRJHK_s$ magnitudes for our Cepheids, the system given by equation (7) can be solved by a linear least-squares method, to find PL coefficients in each band and individual distances and reddenings.

3.2. Random-Phase Correction

The system of equations given by equation (7) assumes that we have phase-average magnitudes in each of our photometric bands. While true for MACHO bands, where we have complete light curves to compute the mean magnitudes, the assumption breaks down for 2MASS: the available quantities are single-epoch JHK_s magnitudes taken at random phases along their respective light curves. Using random-phase NIR magnitudes in equation (7) may still be justified since the amplitudes of pulsations are generally small in the infrared, but having complete light curves in V and R , we can correct for 2MASS random phases and thus improve the accuracy.

Several methods to convert random-phase magnitudes to mean magnitudes have been described in the literature. Freedman (1988) introduced a ‘‘squeeze-and-shift’’ method, which utilizes the similarity of light curves in different photometric bands. According to this method, given a complete light curve in one band (a template), the light curve in any other band can be obtained by scaling the amplitude of the template and introducing a phase lag. A variation of this template-fitting method due to Stetson (1996) is used by the H0KP Team (Gibson et al. 2000) to recover mean I magnitudes from as little as four random-phase data points and the relatively well sampled V -band light curve. Labhardt, Sandage, & Tammann (1997) gave a procedure for finding mean BRI magnitudes from the complete V -band light curve. In essence, their method is very similar to Freedman (1988), except that they allow the phase shift to be variable. The performance of all methods is quite similar, giving the average error for the derived mean of about 0.05 mag. Another way to correct random-phase magnitudes involves Fourier decomposition of light curves

and parameterizing linear relations (interrelations) between Fourier coefficients in different bands (Ngeow et al. 2003). The average error due to such a procedure is also ~ 0.05 mag, but the contaminating effect of bump Cepheids on the relations among Fourier amplitudes is not yet characterized.

Since we have very high quality light curves in both V and R , we are in position to do the random-phase correction straightforwardly. The 2MASS random-phase magnitudes are related to mean NIR magnitudes by

$$m_\lambda(\phi) = \bar{m}_\lambda + \Omega_\lambda(\phi), \quad \lambda = \{J, H, K_s\}, \quad (8)$$

where we introduce a correction term Ω_λ , which is a function of phase of 2MASS observation ϕ . The phase can be derived by overplotting 2MASS data points on top of the MACHO light curve. Mathematically,

$$\phi_i = 2\pi \bmod \left(\frac{T_{2\text{mass},i} - T_{0,i}}{P_i} \right),$$

where $T_{2\text{MASS},i}$ is the Modified Julian Date (MJD) of 2MASS observation, $T_{0,i}$ is the MJD at maximum light in V , and P_i is the period of the Cepheid. Here, as in equation (7), index i denotes different stars in our sample. The correction function $\Omega(\phi)$ is modeled by a low-order Fourier series,

$$\Omega(\phi) = \sum_{j=1}^2 [A_j \cos(2\pi j\phi) + B_j \sin(2\pi j\phi)], \quad (9)$$

which produces correct periodic behavior. Substituting equation (8) into the original system given by equation (7), we derive the expressions for observed random-phase NIR magnitudes:

$$m_{\lambda,i}(\phi_i) = \alpha_\lambda \log P_i + \beta'_\lambda + \Delta\mu_i + R_\lambda \Delta E(B-V)_i + \Omega_\lambda(\phi_i), \quad (10)$$

where $\Omega_\lambda(\phi_i)$ is given by equation (9).

To summarize, our final system of equations is

$$\begin{aligned} \bar{m}_{\lambda,i} &= \alpha_\lambda \log P_i + \beta'_\lambda + \Delta\mu_i + R_\lambda \Delta E(B-V)_i, \\ \lambda &= \{V, R\}, \\ m_{\lambda,i} &= \alpha_\lambda \log P_i + \beta'_\lambda + \Delta\mu_i + R_\lambda \Delta E(B-V)_i \\ &\quad + \Omega_\lambda(\phi_i), \quad \lambda = \{J, H, K_s\}. \end{aligned} \quad (11)$$

For a sample of N stars, the total number of equations is $5N$. The total number of unknowns is $2N + 22$, which includes five pairs of slopes and zero points $(\alpha_\lambda, \beta'_\lambda)$, 12 Fourier coefficients of correction functions Ω_λ (3 bands \times 4 coefficients per function), and distance modulus and reddening offsets for each star, $\Delta\mu_i$ and $\Delta E(B-V)_i$.

3.2.1. Does Phase Correction Really Work?

Table 1 illustrates the effect of the phase-correcting series given by equation (9) in terms of the reduction of scatter for PL relations. The improvement is band dependent, as large as 20% in J , but only $\sim 10\%$ in K_s . This is consistent with amplitudes of pulsation decreasing with wavelength. Furthermore, the reduction of scatter for FO Cepheids is substantially smaller than for FU Cepheids, since the former have smaller amplitudes. The shape of the correction functions Ω_λ is shown in Figures 2 and 3. Both figures show a clear periodic compo-

nent in residual magnitudes that is well fitted by correction functions. Note that the phase of 2MASS observation can be derived from either light curve, V or R , or can be assigned an average value from the two light curves. We have experimented with using V - and R -band phases and mean phases from both light curves and found almost exactly the same results for correction functions. The scatter of the corrected PL relation was marginally smaller for V -band phases, which motivated our choice of V -band phases for the remainder of the paper.

3.3. Error Analysis

The system of equations given by equation (11) models all variations in Cepheid magnitudes as due to distance and reddening only. This is not completely correct: the scatter in PL relations has four main causes: (1) intrinsic variations due to the ε term in equation (3), (2) distance, (3) reddening, and (4) photometric measurement and calibration errors. Another source of error that applies to 2MASS magnitudes only is the random-phase error. This error is suppressed by our phase-correcting technique (see § 3.2), but small residual error due to imperfections of phase correction still remains. In addition, errors in period also contribute to the observed PL scatter by moving points in the diagram in horizontal direction, but these errors are very small, $\sigma_P/P \lesssim 10^{-4}$, and can be safely ignored. Assuming that all these errors are independent of each other, the combined variance of observed PL relations is given by

$$\sigma^2 = \sigma_0^2 + \sigma_\mu^2 + \sigma_{\text{red}}^2 + \sigma_{\text{phot}}^2 + \sigma_{\text{cor}}^2(\text{NIR}). \quad (12)$$

Here we explicitly state that phase correction error applies to NIR magnitudes only. The correction error σ_{cor} can be conservatively estimated at 0.05 mag (we expect that given the quality of 2MASS photometry and MACHO light curves, our method is at least as good as other phase-correcting techniques). The measurement error σ_{phot} is known and includes both random measurement errors and systematic error due to calibration. Since distance and reddening are solved for explicitly, this leaves intrinsic error σ_0 the only unknown. We assigned σ_0 a numerical value of 0.05 mag, independent of photometric band. The results are not very sensitive to the choice of σ_0 : changing it by 0.05 mag results in 0.5 variations in disk position angle and only 0.1 variations in disk inclination.

In practice, the system given by equation (11) is solved in two iterations, where each iteration has two steps. The first iteration deals with observed $VRJHK_s$ magnitudes. At the first step, we evaluate $\alpha_\lambda, \beta'_\lambda, \{A, B\}_j$ by fitting observed PL relations. The fits are done using the unweighted method, i.e., using magnitudes without uncertainties. Once the PL coefficients are derived, we solve for distance and reddening to each individual star. This time, the least-squares method is weighted by inverse variance, with variance now incorporating propagated errors from the PL fit at first step:

$$\sigma_i^2 = \sigma_0^2 + \sigma_{\text{phot}}^2 + \sigma_{\text{cor}}^2(\text{NIR}) + \sigma_a^2 \log^2 P_i + \sigma_b^2.$$

The variance also includes intrinsic and photometric errors, as well as phase correction errors for NIR magnitudes. The solution gives offset quantities $\Delta\mu_i, \Delta E(B-V)_i$, relative to mean LMC values. The estimators for PL slope and zero point, as well as correction function coefficients, obtained at first step, are held fixed. This constitutes the first iteration. On the second iteration, we correct observed magnitudes for distance and

TABLE 1
RESULTS OF THE RANDOM-PHASE CORRECTION

Band	σ_r (Random Phase)	σ_c (Corrected)	$(\sigma_r - \sigma_c)/\sigma_r$
FU Cepheids			
J	0.161	0.129	0.20
H	0.133	0.114	0.14
K_s	0.142	0.129	0.09
FO Cepheids			
J	0.135	0.127	0.06
H	0.118	0.115	0.03
K_s	0.137	0.134	0.02

reddening and redo the same two steps again. (Note that the magnitudes are corrected only for differential quantities $\Delta\mu_i$ and $\Delta E(B-V)_i$, which may vary from star to star, while the effect of the total line reddening is not taken out.) This gives us the improved PL relation, where effects of varying distance moduli and reddenings are taken out. The values for reddenings and distance moduli obtained at the second iteration are essentially noise. The solutions (two iterations) for FU and FO Cepheids are obtained separately, but after distances are derived we put both samples together to derive viewing angles of the LMC disk.

4. RESULTS

4.1. PL Relations

The results for linear PL fits are presented in Tables 2 and 3 for FU and FO Cepheids, respectively. Each table lists results from both iterations, with and without distance/reddening

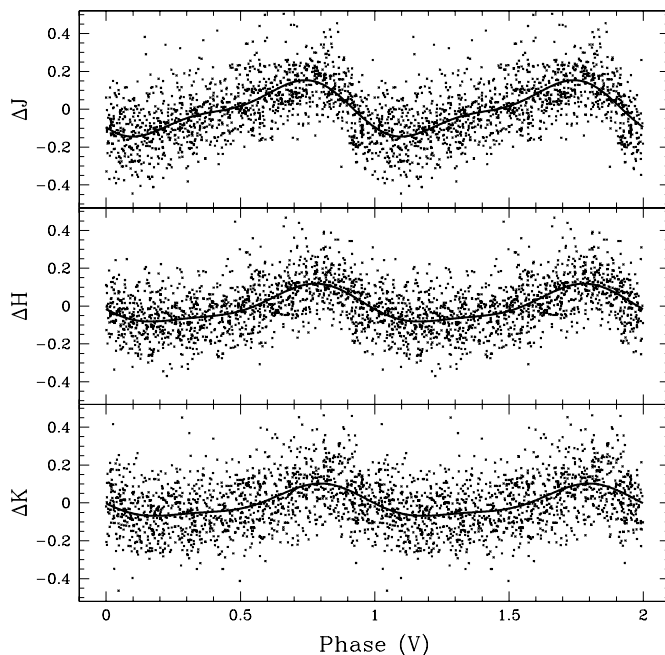


FIG. 2.—Correction functions $\Omega_i(\phi)$ for FU-mode Cepheids. Top to bottom, panels show the correction functions in J , H , and K_s . Crosses represent differences between observed magnitude and the fitted PL relation for each individual Cepheid. Overplotted solid lines show the correction functions. Note the increasing flatness of the curves from J to K_s , which is due to decreasing pulsation amplitudes. Also visible is the phase lag at maximum light.

correction. Corresponding plots are shown in Figures 4 and 5. The figures suggest that reddening plays a significant role in the dispersion of observed PL relations, as there is a clear gradient in the scatter from band to band. The errors in VR bands are clearly dominated by reddening and distance, while in NIR bands the main contributors to scatter are photometric and phase correction errors.

It has been a common practice in the literature (Udalski et al. 1999; Groenewegen 2000) to employ an iterative k - σ clipping method to clean the PL relations from outliers. The method does PL fitting iteratively, removing data points outlying by more than k standard deviations from the current best-fitting line between iterations. The iterations stop when the number of points does not change. Unfortunately, the method relies on the assumption that errors are distributed normally, which is not the case for distances and reddenings, as can be seen from Figures 4 and 5. In addition, the method is rather sensitive to the arbitrarily selected clipping constant k . Rather than using the k - σ clipping, we adopted a different approach: after computing the best-fitting PL relations and solving for distances and reddenings, we removed those outlier Cepheids that were a significant distance away from the disk. The cutoff distance was taken at 7 kpc, so that all outliers are at least 3σ significant. Altogether, we found 44 outliers: 33 “in front of” and 11 “behind” the main LMC disk. The outliers deserve a very close second look, since they can help to resolve the discrepancy between the observed microlensing event rate and that predicted by models. We plan to study them in more detail later.

It is important to note that the removal of outliers was done before obtaining solutions, so that PL relations in Tables 2 and 3 and Figures 4 and 5 do not have the outlier points. As a consequence, the derived viewing angles are also unaffected by the distance outliers.

4.2. Distance Moduli and Reddenings for Individual Cepheids

Once mean observed PL relations are obtained, we fit their residuals with variations in distance modulus and reddening,

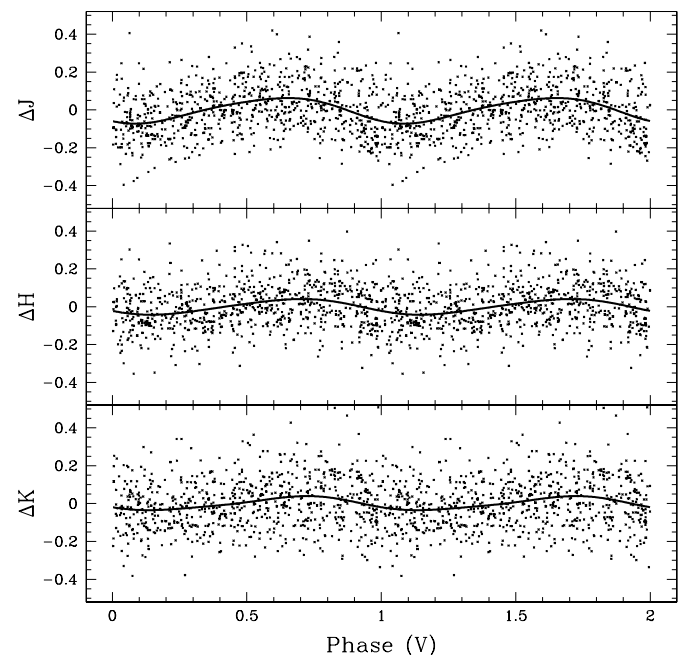


FIG. 3.—Same as Fig. 2, except for FO-mode Cepheids. Note the smaller amplitude of the correction functions, which is due to smaller pulsation amplitudes for FO Cepheids.

TABLE 2
FITTED PL RELATIONS FOR FUNDAMENTAL-MODE CEPHEIDS

Band	α_λ	β'_λ	σ_{fit}
Iteration 1			
V.....	-2.616 ± 0.038	17.444 ± 0.025	0.280
R.....	-2.780 ± 0.033	17.161 ± 0.021	0.239
J.....	-3.068 ± 0.018	16.389 ± 0.011	0.129
H.....	-3.180 ± 0.016	16.121 ± 0.010	0.114
K _s	-3.175 ± 0.018	16.038 ± 0.011	0.129
Iteration 2			
V.....	-2.615 ± 0.002	17.443 ± 0.002	0.018
R.....	-2.782 ± 0.003	17.162 ± 0.002	0.023
J.....	-3.074 ± 0.006	16.394 ± 0.004	0.044
H.....	-3.187 ± 0.007	16.128 ± 0.004	0.049
K _s	-3.183 ± 0.010	16.045 ± 0.007	0.074

NOTE.—Iteration 1 refers to the PL fits to raw data, while iteration 2 refers to the fits to data corrected for distances and reddenings (see § 3.3) Note that the effect of the mean line reddening, $\overline{E(B - V)}_{\text{LMC}}$, has not been taken out in data for iteration 2.

i.e., the remaining terms in equation (11). The form of equation (11) suggests that the resulting values for $\Delta\mu_i$ and $\Delta E(B - V)_i$ will be anticorrelated because the method constrains their sum. This leads to a particular signature in the $[\Delta\mu, \Delta E(B - V)]$ -plane, where larger distances correspond to smaller reddenings (see Fig. 6). For any reasonable LMC model with a dust layer, the expected behavior is exactly the opposite of what is observed: stars at greater distances should have greater reddening. Figure 6 does show a hint of extension toward larger distances and larger reddenings, but the effect is deteriorated by correlated errors in $\Delta\mu$ and $\Delta E(B - V)$. In our method, median distance modulus error is 0.072 mag, while median reddening error is 0.042 mag. The error bars in Figure 6 should really be tilted so that the main axes of the individual error ellipses are aligned with the scatter ellipsoid. A projection of the results on the reddening axis gives a distribution of reddenings quite consistent with Harris, Zaritsky, & Thompson (1997): the distribution is markedly

non-Gaussian, with a long tail extending toward high reddenings, up to 0.6–0.7 mag above the mode.

Figure 7 shows the reddening offsets as a function of period. This diagram addresses a valid concern that our derived reddenings may have systematic effects due to the Cepheid “period-color” relation. By using PL relations in our method (ignoring intrinsic colors) and modeling magnitude residuals by variations in distance and reddening only, we could have overestimated reddenings for long-period stars and underestimated them for short-period Cepheids. A look at Figure 7 shows that this is not the case. The fit line (shown) has both slope and zero point consistent with zero at the 1 σ level.

4.3. Mean LMC Distance Modulus and Reddening

The values derived from solving equation (11), $\Delta\mu_i$ and $\Delta E(B - V)_i$, are offsets from the mean reddening and distance modulus of the LMC. To obtain physically meaningful quantities, they have to be adjusted by their respective mean LMC

TABLE 3
FITTED PL RELATIONS FOR FIRST-OVERTONE CEPHEIDS

Band	α_λ	β'_λ	σ_{fit}
Iteration 1			
V.....	-3.123 ± 0.080	16.990 ± 0.031	0.315
R.....	-3.190 ± 0.069	16.695 ± 0.027	0.272
J.....	-3.323 ± 0.032	15.896 ± 0.013	0.127
H.....	-3.371 ± 0.029	15.629 ± 0.011	0.115
K _s	-3.348 ± 0.034	15.552 ± 0.013	0.134
Iteration 2			
V.....	-3.123 ± 0.005	16.990 ± 0.002	0.019
R.....	-3.193 ± 0.007	16.696 ± 0.003	0.026
J.....	-3.336 ± 0.012	15.904 ± 0.005	0.047
H.....	-3.385 ± 0.014	15.638 ± 0.006	0.056
K _s	-3.363 ± 0.023	15.561 ± 0.009	0.092

NOTE.—Iteration 1 refers to the PL fits to raw data, while iteration 2 refers to the fits to data corrected for distances and reddenings (see § 3.3) Note that the effect of the mean line reddening, $\overline{E(B - V)}_{\text{LMC}}$, has not been taken out in data for iteration 2.

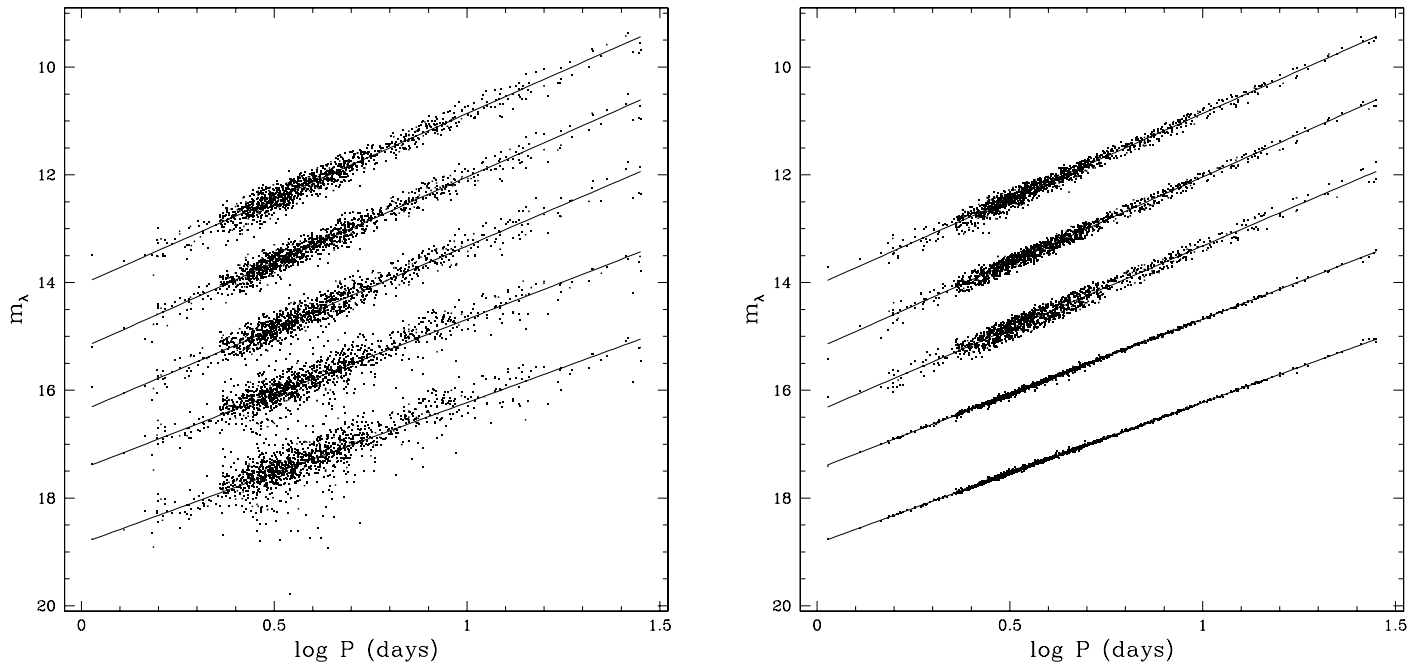


FIG. 4.—PL relations for FU Cepheids. *Left*: Iteration 1 (fitting observed magnitudes). *Right*: Iteration 2 (fitting magnitudes corrected for distance and reddening). Solid lines are fitted PL relations. The PL relations are vertically offset for clarity. The difference in error reduction between optical and NIR bands suggests that scatter in V, R is dominated by distance and reddening variations, while scatter in NIR bands is due to photometric and phase errors.

values (see eq. [6]). Both $\overline{\mu}_{\text{LMC}}$ and $\overline{E(B - V)}_{\text{LMC}}$ are arbitrary constants that cannot be constrained based on our data alone.³ They can be tied to other determinations of distance and reddening by considering common stars or common areas of the LMC. In the next section we give the results of several such calibrations for reddenings only, with the aim of presenting the LMC reddening map. The mean LMC distance will not

³ The mean reddening $\overline{E(B - V)}_{\text{LMC}}$ is in fact somewhat constrained by requiring reddenings to be nonnegative.

be calibrated here because knowing absolute distances to Cepheids is irrelevant for viewing angles. We stress that neither of the mean values has any impact on the main results in § 4.4: the viewing angles are completely independent of adopted values for $\overline{E(B - V)}_{\text{LMC}}$ and $\overline{\mu}_{\text{LMC}}$.

4.3.1. Mean Reddening

Our main goal in calibrating mean LMC reddening is producing a reddening map of the LMC. The values of mean LMC reddening (combined with foreground reddening) found in the

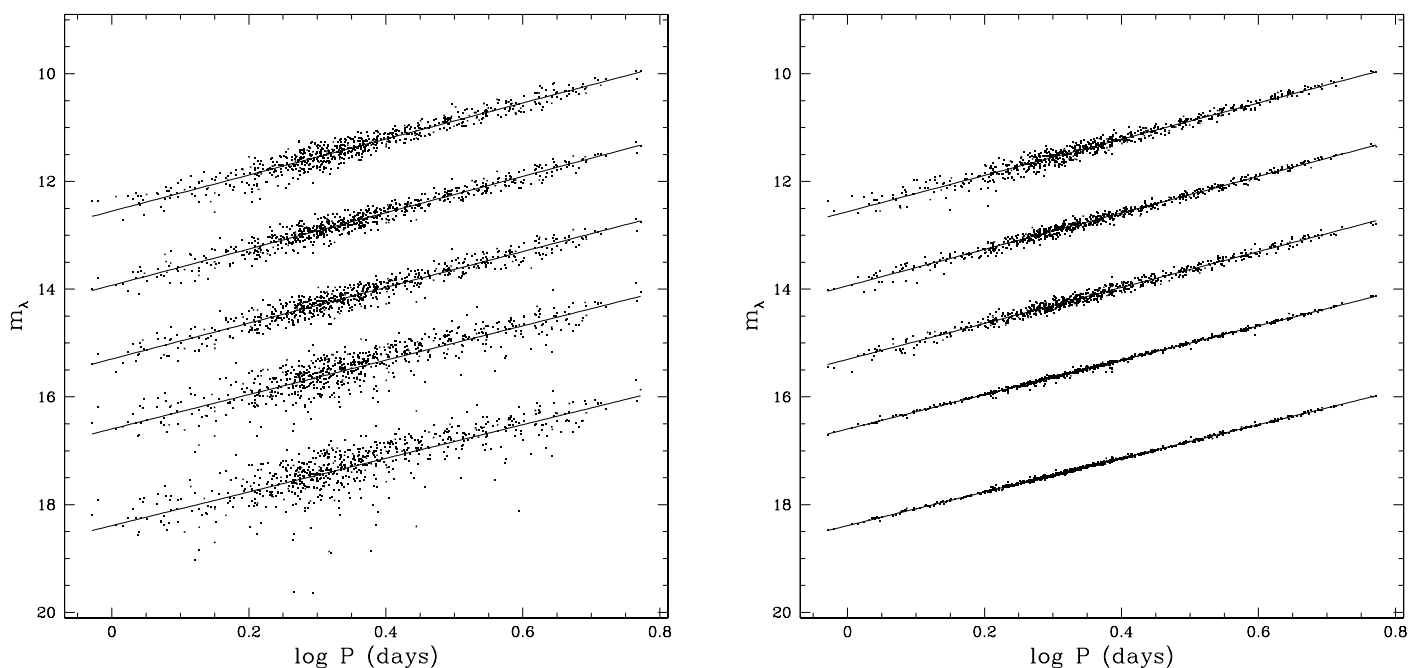


FIG. 5.—PL relations for FO Cepheids. The panels are as in Fig. 4. The relations are vertically offset for clarity.

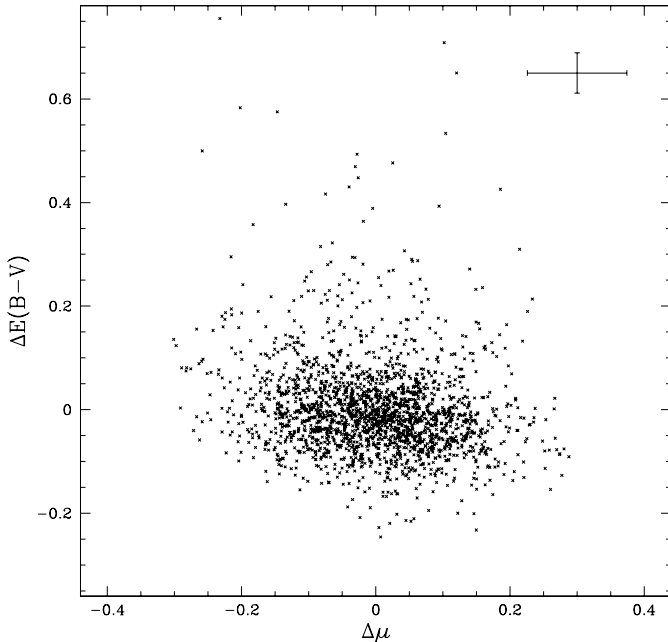


FIG. 6.—Reddening values vs. distance moduli for all Cepheids in our sample (FU and FO). Note the apparent anticorrelation in values, which is due to the particular form of eq. (7). Typical size of the error bars for individual points is shown in the upper right-hand corner.

literature span a significant range: from $\overline{E(B-V)} = 0.074$ (Caldwell & Coulson 1985) to $\overline{E(B-V)} = 0.20$ (Harris et al. 1997). As noted by Zaritsky (1999), some of the discrepancy can be explained by stellar population effect: values of reddening derived from early-type stars may be biased high, as a result of their preferential location in dusty star-forming regions. In addition, the dust distribution within the LMC is clumpy, with variations on the scale of a few arcseconds (Harris et al. 1997).

We estimate the mean $E(B-V)$ reddening by three different methods:

1. Comparison with theoretical pulsation models. One can use Cepheid pulsation models to infer physical parameters of stars, as well as their distance and reddening. Recently, Keller & Wood (2002) used theoretical models on a sample of about 20 bump Cepheids from MACHO data archives. Fitting the observed light curves, they derived pulsation masses, luminosities, and effective temperatures for each Cepheid, which can be converted to distances and reddenings. Because the bump Cepheids are also taken from MACHO data, there is no systematic difference in photometry (we are using the same light curves). The internal reddening errors of their method are 0.01, but the systematic error from MACHO photometry carries over. Since all of their Cepheids are in MACHO “top 30” fields, they have a systematic error of 0.035 mag. By comparing the absolute reddenings for these bump Cepheids with relative reddenings for the same stars derived by our statistical approach, we can derive the mean reddening that minimizes the differences. The derived value is $\overline{E(B-V)} = 0.16 \pm 0.04$, and the comparison of the two samples is shown in Figure 8. The method also permits absolute calibration of the mean distance modulus, which turns out to be $\overline{\mu} = 18.57 \pm 0.13$.

2. Matching with mean star formation history (SFH) reddenings in *HST* WFPC2 fields. A set of mean reddenings for selected *HST* fields in the LMC was obtained by C. Nelson

(2002, private communication). The reddenings were derived using SFH code (Harris & Zaritsky 2001) on *HST* color-magnitude diagrams. To compare the reddenings, we selected all Cepheids within 15' of the *HST* field centers and computed variance-weighted averages of their relative reddening values. Calculating the mean shift required to match average reddenings of the two sets gives $\overline{E(B-V)} = 0.12 \pm 0.04$. The results are shown in Figure 8.

3. Locating zero point for reddening distribution. A weak constraint on mean reddening results from requiring non-negative individual reddenings (within errors). This is a very crude method, but it provides at least some measure of $\overline{E(B-V)}$. The method depends on the assumed fraction f_0 of “zero-reddening” stars in our sample, i.e., stars with low true reddening that are scattered into negative reddenings by statistical errors. By selecting the fraction f_0 and shifting the entire distribution along the horizontal axis so that the corresponding percentile is at zero, we obtain mean reddening of our sample. For $f_0 = 0.01$, we derive $\overline{E(B-V)} = 0.16$, while for $f_0 = 0.05$, the mean reddening is $\overline{E(B-V)} = 0.11$. Assuming that zero-reddening stars constitute less than 5% of our sample, the mean reddening is $\overline{E(B-V)} = 0.14 \pm 0.03$.

All three above estimates of mean LMC reddening are consistent with each other, despite completely different ways of obtaining them. Their variance-weighted average is $\overline{E(B-V)} = 0.14 \pm 0.02$. While this seems higher than most estimates based on Cepheids, e.g., 0.074 ± 0.007 (Caldwell & Coulson 1985), it agrees well with the mean value from 84 lines of sight from OGLE, $E(B-V) = 0.137$ (Udalski et al. 1999), and mean reddening of 0.16 derived by Oestreich & Schmidt-Kaler (1996) from photometry of OB stars.

4.3.2. Reddening Map of the LMC

Figure 9 shows the reddening maps of the LMC on a rectangular grid. To produce the (α, δ) -map, we binned the observed LMC area on a 10×10 grid and computed weighted

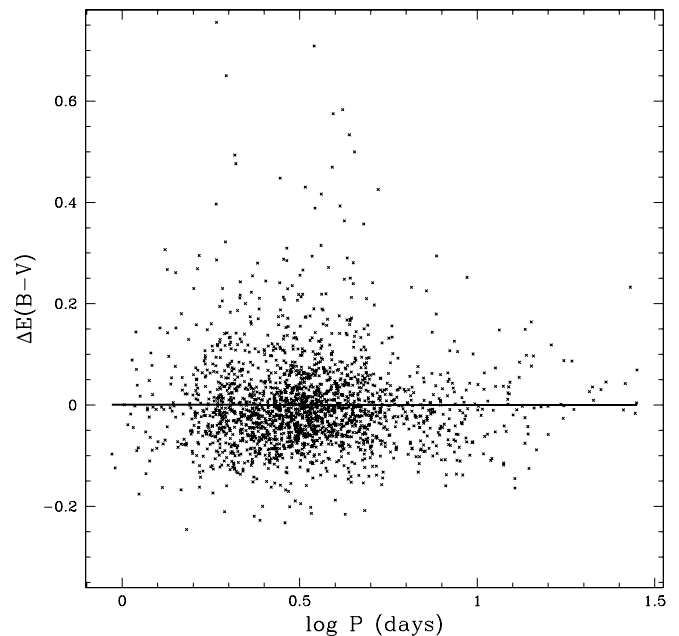


FIG. 7.—Individual Cepheid reddening offsets as a function of their period. The solid line shows the least-squares fit, with both zero point and slope consistent with zero. This suggests no systematic effect due to ignored PL relation.

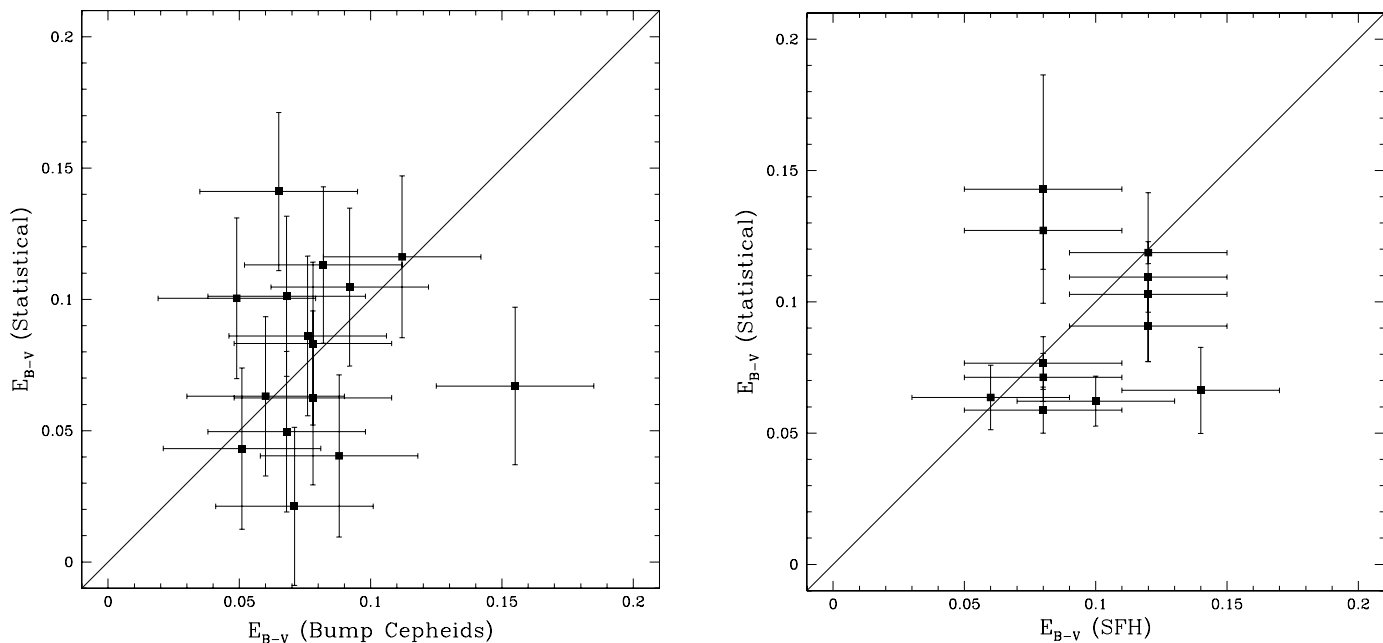


FIG. 8.—Calibration of the reddening zero point $\overline{E(B - V)}$ based on theoretical models of bump Cepheids (*left*) and *HST* WFPC2 fields (*right*). The differential reddenings derived from eq. (11) were shifted by 0.16 (*left*) and 0.12 (*right*), according to the mean zero point from each method. Straight lines in both panels show one-to-one dependence.

averages for Cepheids in each spatial bin. Each bin also displays the statistical uncertainty of the estimate. The values in the map have been converted to absolute reddenings, using $\overline{E(B - V)} = 0.14$. To better visualize the reddening structure, Figure 9 also shows the density map of reddening, with overlaid contour levels. The density map was obtained by averaging Cepheid reddening on a 40×40 grid and smoothing the resulting distribution with a circular Gaussian kernel ($\sigma_x = \sigma_y = 1$ kpc). The most prominent feature in the

figure is the high-reddening region near $\alpha \sim 86^\circ$, $\delta \sim -69^\circ$ ($x_0 \sim -1.8$, $y_0 \sim -1$). The region is probably associated with 30 Doradus and supergiant shells LMC2 and LMC3 (Martin et al. 1976), even though 30 Dor itself was not observed by MACHO. Also visible in the map are both northwest and southeast spiral arms. The maps in Figure 9 are in good agreement with the far-infrared maps of Schwering (1989) and maps of H I column density (Luks & Rohlfs 1992).

			0.048	0.133				
			0.019	0.022				
-66		-0.017	0.161	0.146	0.083	0.112	0.074	0.152
		0.024	0.022	0.008	0.007	0.006	0.014	0.018
		0.139	0.150	0.159	0.108	0.138	0.096	0.164
		0.011	0.011	0.009	0.007	0.006	0.007	0.018
68	0.054	0.049	0.099	0.133	0.083	0.109	0.121	0.097
	0.043	0.008	0.006	0.007	0.012	0.022	0.010	0.006
	0.051	0.078	0.180	0.158	0.173	0.155	0.123	0.121
	0.016	0.012	0.009	0.008	0.011	0.009	0.005	0.005
	0.029	0.152	0.319	0.224	0.168	0.123	0.129	0.113
	0.042	0.010	0.009	0.008	0.006	0.004	0.004	0.004
-70		0.102	0.216	0.238	0.132	0.127	0.102	0.075
		0.015	0.006	0.003	0.003	0.003	0.006	0.008
		0.208	0.185	0.099	0.089	0.105	0.127	0.155
		0.006	0.004	0.008	0.005	0.006	0.009	0.010
-72		0.270	0.192	0.147	0.125	0.092	0.116	0.089
		0.059	0.012	0.012	0.007	0.011	0.010	0.012
		0.071	0.075	0.127	0.304			
		0.044	0.022	0.025	0.045			
		90	85	80	75	70		

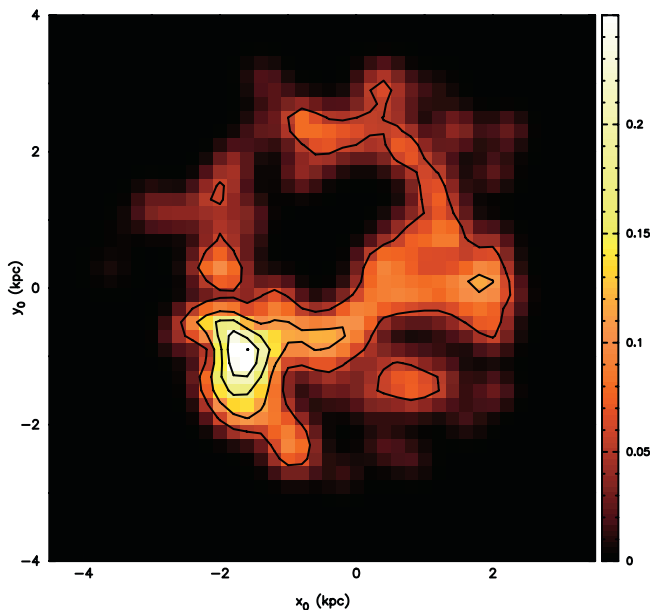


FIG. 9.—*Left*: Reddening distribution for LMC Cepheids. Data are binned on a 10×10 coordinate grid. In each bin, we compute weighted averages and standard deviations, using $\overline{E(B - V)} = 0.14$. *Right*: Reddening map of the LMC, derived from Cepheids. To produce the map, we computed average reddening on a 40×40 grid in (x_0, y_0) -coordinates and used Gaussian smoothing with $\sigma_x = \sigma_y = 1$ kpc. Contour levels are spaced by 0.05 mag. In both panels the high-reddening zone near 30 Dor ($\alpha \sim 86^\circ$, $\delta \sim -69^\circ$) is clearly visible.

Note that for a random location in the map, reddening is likely to be less than the mean value $\overline{E(B-V)} = 0.14$, as a result of the extended tail of the distribution. The mode of the distribution is displaced by $\Delta E(B-V) = -0.02$ mag from the mean.

4.4. Viewing Angles of the LMC Disk

To obtain inclination and position angle of the LMC disk, we use individual Cepheid distances derived from equation (11). These distances are plotted in Figure 10, projected on coordinate axes. The figure clearly shows the drift in magnitudes, which is due to the slope of the LMC disk. The overall slope in the figure indicates that the closest part of the disk is the northeast part. To calculate the orientation of the main disk, we fit a plane solution to the individual distance moduli,

$$z_{0,i} = Ax_{0,i} + By_{0,i} + C, \quad i = 1, N, \quad (13)$$

where $\{x_0, y_0, z_0\}$ are star coordinates in the coordinate system of Weinberg & Nikolaev (2001; see their § A1). The transformation from $\Delta\mu$ to real physical coordinates $\{x_0, y_0, z_0\}$ requires a fixed point (the origin of the coordinate system), defined by three parameters: the sky coordinates α_0, δ_0 and the distance R_0 . In addition, one needs to know the mean LMC distance modulus $\bar{\mu}_{\text{LMC}}$, to convert relative distance offsets $\Delta\mu_i$ to physical units. For our model, we adopt a ‘‘canonical’’ value used by the HOKP Team, $\bar{\mu}_{\text{LMC}} = 18.5 \pm 0.1$ (Madore et al. 1999). Parameter C in equation (13) is necessary to eliminate bias due to arbitrariness in R_0 : the constant would be zero if the origin of our coordinate system were exactly at the real center of the LMC disk. From slopes A and B it is easy to compute position angle θ and inclination i of the disk:

$$\theta = \arctan\left(-\frac{A}{B}\right) + \text{sign}(B)\frac{\pi}{2},$$

$$i = \arccos\left(\frac{1}{\sqrt{1+A^2+B^2}}\right).$$

The solution to equation (13) is obtained by a least-squares method and is a function of the adopted LMC center (α_0, δ_0) . Changing R_0 only affects C and does not change θ and i .

The inferred position angles and inclinations for several models are presented in Table 4. Our ‘‘default’’ model, which assumes the H I rotation center as the coordinate system origin, $(\alpha_0, \delta_0) = (79^\circ.40, -69^\circ.03)$, has (solution 3 in Table 4)

$$\theta = 151^\circ.0 \pm 2^\circ.4, \quad i = 30^\circ.7 \pm 1^\circ.1.$$

5. DISCUSSION

5.1. Comparison to Previous Results

A study of this magnitude, using five-color photometry of more than 2000 Cepheids, covering ~ 60 deg² of the LMC, is unprecedented. It should be considered the most accurate analysis of the inner LMC to date. Our results validate many of the previous measurements derived from Cepheids. Caldwell & Coulson (1986) analyzed a sample of 73 Cepheids and obtained $i = 28^\circ.6 \pm 5^\circ.9$, $\theta = 142^\circ.4 \pm 7^\circ.7$, both values consistent with our results at the 1σ level. Laney & Stobie (1986) used *JHK* photometry of 21 LMC Cepheids to derive $i = 45^\circ \pm 7^\circ$, $\theta = 145^\circ \pm 17^\circ$, although their results could have been affected by particular sky distribution of their Cepheids and small number statistics. Welch et al. (1987) derived $i = 37^\circ \pm 16^\circ$, $\theta = 167^\circ \pm 42^\circ$, which is also consistent with our estimate (because of large error bars, their results are consistent with virtually all existing estimates of the LMC viewing angles). Recently, Groenewegen (2000) examined combined OGLE and 2MASS photometry for 825 Cepheids in the bar of the LMC. The study attempted to derive the viewing angles of the LMC by fitting a plane solution to the reddening-free Wesenheit index, $W = I - 1.55(V-I)$. Despite the large sample, the results in Groenewegen (2000) should be taken with caution, since viewing angles are derived from data in the bar only. Being essentially a one-dimensional structure, the bar cannot effectively constrain both the inclination and the line of nodes of the

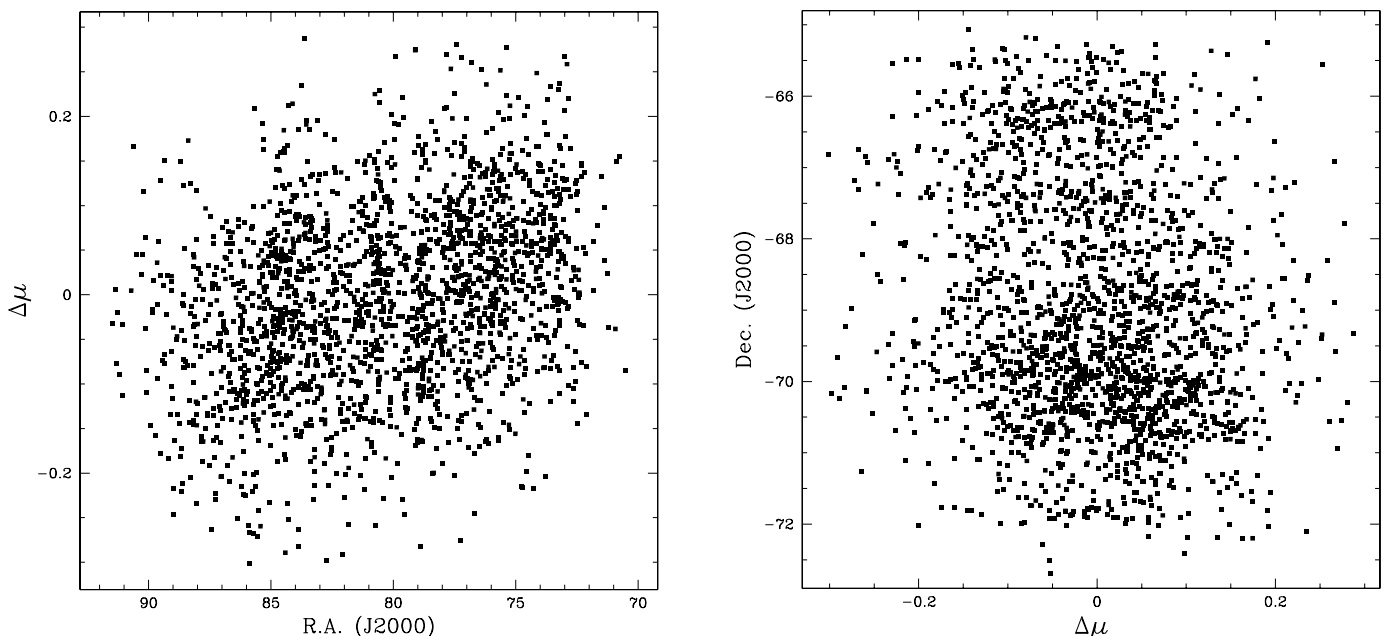


FIG. 10.—Distance moduli (offsets) for individual Cepheids as functions of spatial coordinates. The results for FU and FO Cepheids are combined. The linear drift in magnitudes is clearly visible and corresponds to the main LMC disk. The error bars on the distance moduli are not shown, to make the plot less crowded; the typical error in distance modulus is ~ 0.1 mag.

TABLE 4
VIEWING ANGLES FOR INCLINED DISK LMC MODELS

Solution	θ (deg)	i (deg)	Reduced χ^2	Remarks
$(\alpha_0, \delta_0) = (79^\circ.4, -69^\circ.03)^a$				
1.....	154.4 ± 3.0	30.3 ± 1.3	1.88	FU only
2.....	144.3 ± 4.1	31.8 ± 1.8	1.38	FO only
3.....	151.0 ± 2.4	30.7 ± 1.1	1.71	FU and FO combined
$(\alpha_0, \delta_0) = (80^\circ.4, -69^\circ.0)^b$				
4.....	153.7 ± 3.0	30.6 ± 1.3	1.87	FU only
5.....	143.6 ± 4.0	32.0 ± 1.8	1.37	FO only
6.....	150.2 ± 2.4	31.0 ± 1.1	1.70	FU and FO combined
$(\alpha_0, \delta_0) = (82^\circ.25, -69^\circ.5)^c$				
7.....	153.3 ± 3.0	30.9 ± 1.3	1.86	FU only
8.....	142.8 ± 4.0	32.1 ± 1.8	1.37	FO only
9.....	149.8 ± 2.4	31.2 ± 1.1	1.68	FU and FO combined

^a Rotation center of the LMC as inferred from H I data (Kim et al. 1998).

^b Geometric center of our sample.

^c Center of carbon star outer isopleths, as given by MC01.

LMC disk. In addition, the viewing angles were derived solely from V, I OGLE data, ignoring NIR photometry. Olsen & Salyk (2002) examined red clump magnitudes in the inner LMC and derived $i = 35^\circ.4 \pm 2^\circ.3$, $\theta = 142^\circ \pm 4^\circ$. All these estimates derive viewing angles from tracer magnitude variations, in contrast to isophotal and isoplethic methods that typically derive higher position angles, $\theta \sim 170^\circ - 190^\circ$ from apparent aspect ratio. One recent analysis (MC01) used modal magnitudes of color-selected asymptotic giant branch (AGB) carbon stars from DENIS and 2MASS to obtain a new estimate, $i = 34^\circ.7 \pm 6^\circ.2$, $\theta = 122^\circ.5 \pm 8^\circ.3$. While the value for inclination is similar to many previous estimates, the derived position angle of the line of nodes is unusually low. A similar result was obtained by van der Marel et al. (2002) from kinematics of LMC carbon stars, $\theta = 129^\circ.9 \pm 6^\circ.0$. This low value of the position angle was used as evidence that LMC is highly elliptical. We offer a detailed comparison of the MC01 analysis and ours in the next two sections.

5.2. Sensitivity of Results to Adopted Parameters

As stated above, our plane-fitting algorithm has a number of free parameters, including position of the coordinate origin (α_0, δ_0) and mean LMC distance modulus, $\bar{\mu}_{\text{LMC}}$. The mean LMC distance modulus does not affect viewing angles: changing $\bar{\mu}_{\text{LMC}}$ simply scales the size of the disk while preserving its orientation. The position of the LMC center, on the other hand, does have an effect on inclination and especially position angle. In Table 4 we present results for three choices of coordinate origin: (1) center defined by H I rotation map (Kim et al. 1998), $(\alpha_0, \delta_0) = (79^\circ.4, -69^\circ.03)$, (2) geometric center of our Cepheid sample, $(\alpha_0, \delta_0) = (80^\circ.4, -69^\circ.0)$, and (3) center of outer carbon star isopleths as given by MC01, $(\alpha_0, \delta_0) = (82^\circ.25, -69^\circ.5)$. All three centers are within 2° of each other. From the table, we observe that both the inclination and the position angle vary by a few degrees, depending on the choice of origin.

Figure 11 gives an expanded view of the sensitivity to coordinate origin. To make the figure, we ran our plane-fitting

algorithm for a grid of origin locations, by varying α_0 from 79° to 83° and δ_0 from $-70^\circ.5$ to $-68^\circ.5$. For each choice of the LMC center, we obtained a planar solution to equation (13), using our entire Cepheid sample. The figure suggests a very slight dependence on the adopted coordinate origin: for any reasonable choice for the LMC center, variations in derived parameters are limited to $\lesssim 4^\circ$ for position angle and $\lesssim 3^\circ$ for inclination. (The dependence is due to the curvature of the sky.) While noticeable, the effect seems not strong enough to explain the MC01 result. However, we note that results in Table 4 and Figure 11 are based on the entire sample of stars, while MC01 used smaller concentric rings to derive their solution. Their analysis split the LMC disk into radial zones and obtained viewing angle solutions for each radial zone, allowing for parameter variability from zone to zone. The stars within $2^\circ.5$ of the center were excluded.

To reproduce the results of MC01, we use the same concentric radial zones. Their first radial ring (hereafter R1) extends from $2^\circ.5$ to $3^\circ.4$ from the center. Figure 12 shows the viewing angles derived for a grid of center locations, where for each center we repeat the fitting procedure described in § 4.4 using only Cepheids (both FU and FO) from the first MC01 radial ring. The grid is the same as in Figure 11, but the results are remarkably different. Now we see a very strong sensitivity to the location of the adopted LMC center. For example, moving the origin by a mere 2° can change the position angle by 35° ! In particular, for the MC01 origin, we derive $\theta = 127^\circ.2 \pm 4^\circ.5$ and $i = 30^\circ.6 \pm 2^\circ.0$ (from 531 stars), i.e., position angle very similar to the MC01 result. On the other hand, using R1 data with H I rotation center gives $\theta = 153^\circ.6 \pm 3^\circ.2$ and $i = 34^\circ.0 \pm 1^\circ.6$ (from 615 stars), i.e., very close to our “global” LMC values from § 4.4. The same analysis can be repeated for the second radial ring of MC01, which extends from $3^\circ.4$ to $4^\circ.4$ from the center. Repeating the calculations, we find $\theta = 118^\circ.1 \pm 9^\circ.3$, $i = 26^\circ.3 \pm 3^\circ.5$ (from 323 stars) for the MC01 origin and $\theta = 147^\circ.4 \pm 10^\circ.5$, $i = 22^\circ.7 \pm 3^\circ.8$ (from 173 stars) for H I rotation center. Note that the errors on

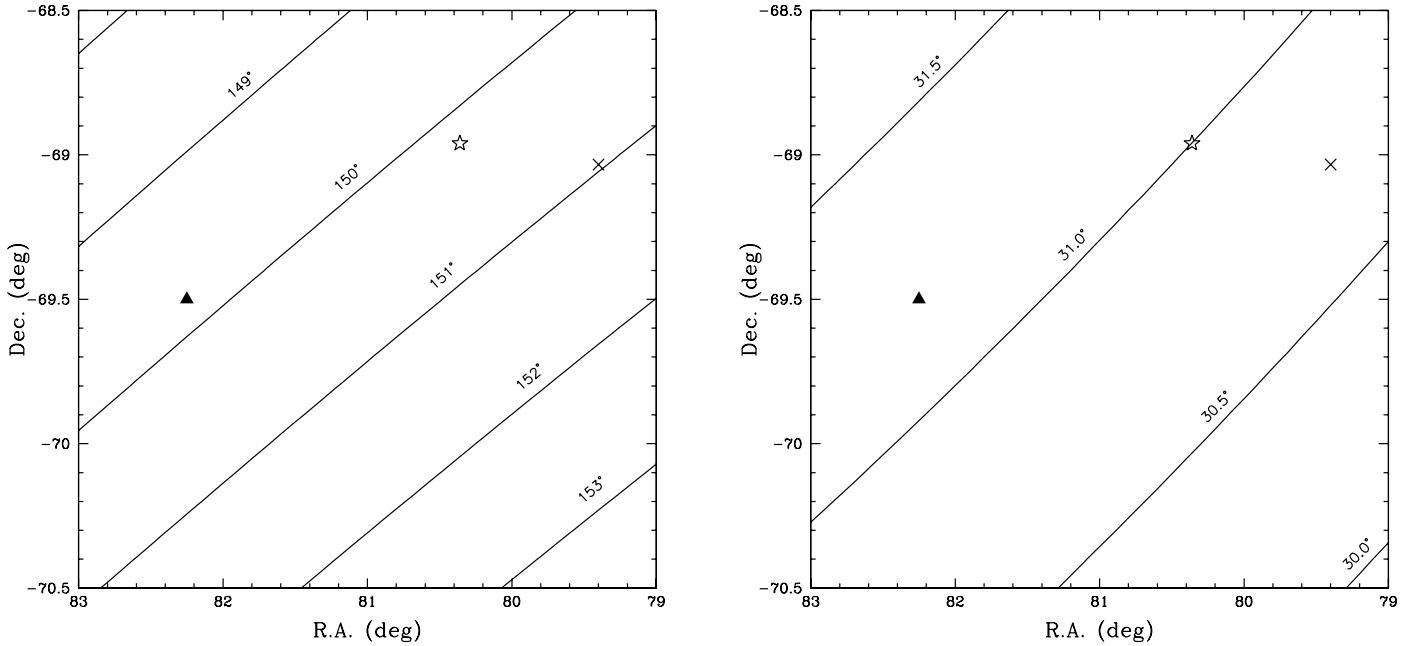


FIG. 11.—Variations in the viewing angles of the LMC due to choice of the coordinate origin. The viewing angles are derived from the entire sample. *Left:* Inferred position angles. *Right:* Inclinations. The cross indicates the H I rotation center according to Kim et al. (1998), the star shows the geometric center of our Cepheid sample, and the triangle gives the center of carbon star isopleths from MC01.

the estimates have increased significantly because there are fewer stars in the second ring.

The reason for such a strong dependence on the LMC origin is clearly a selection effect: depending on the origin, the stars constituting the ring will change. We interpret Figure 12 as evidence for nonplanar material in the inner LMC. Indeed, if all stars were in the same plane, the choice of the origin would have a small effect on derived viewing angles, at most a few degrees in i and θ , as a result of curvature of the sky. Inversely, if ring analysis does depend on the choice of the LMC center, some stars must be out of the plane. The difference between

our results for the entire sample (low sensitivity to origin position) and for the radial rings (high sensitivity) is due to the fact that the ring analysis is sensitive to variations in the distance moduli on a small angular scale, while using the entire data set “smoothes” them out. To illustrate this, Figure 13 shows both distance offsets and the expected signal from inclined disk (*solid line*), for three cases: (1) R1 centered at the H I rotation center, (2) R1 centered at the MC01 origin, and (3) full plane centered at the MC01 origin. The distance offsets are converted from distance moduli to kiloparsecs. To make the signature more obvious, we bin the data by 45° bins and

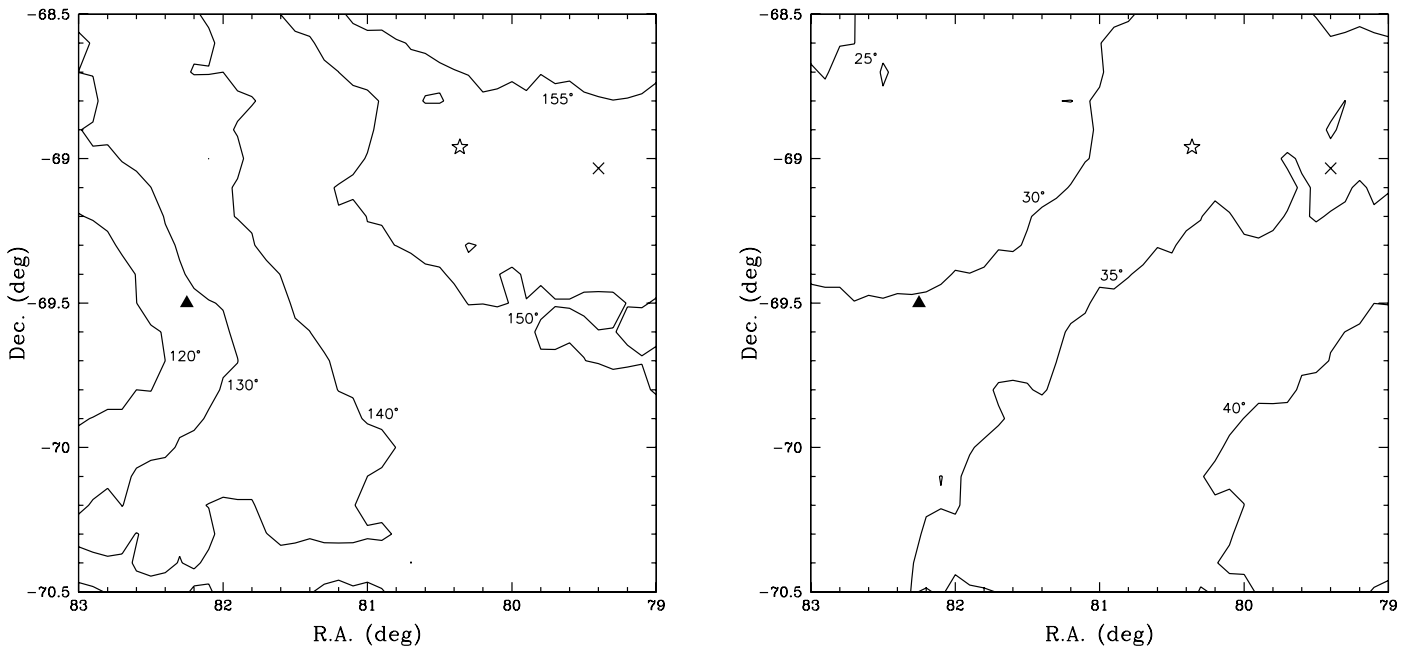


FIG. 12.—Same as Fig. 11, except viewing angles are derived from the ring of stars, $2.5 < \rho < 3.4$ from the origin. The contour levels are labeled in degrees, and the symbols are as in Fig. 11.

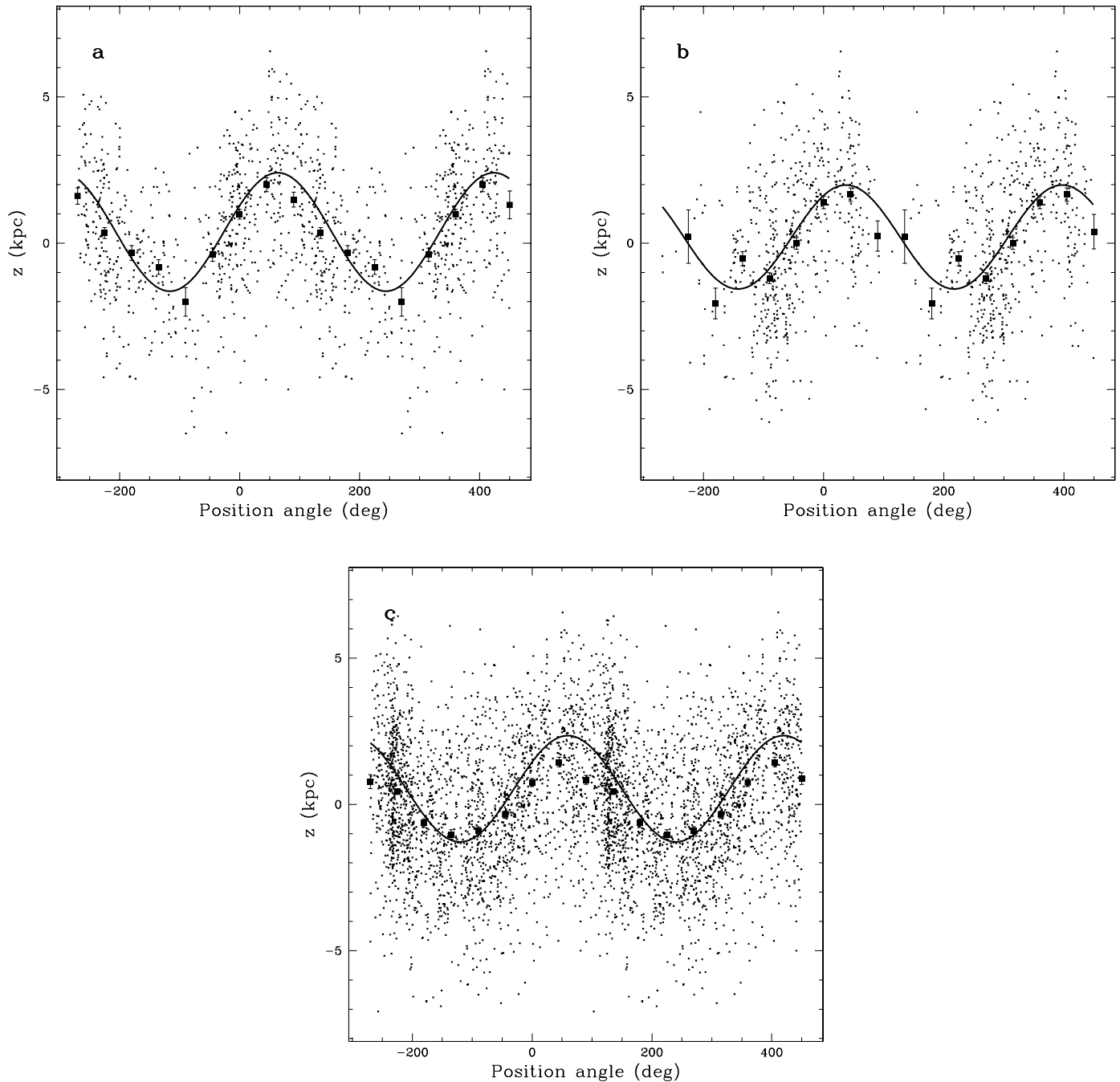


FIG. 13.—Distance offsets (z -coordinate) and expected signal from inclined disk (*solid line*) for three models: (*a*) first radial ring and H I rotation center, (*b*) first radial ring and MC01 center, and (*c*) full plane and MC01 origin (solution 9 in Table 4). Points with error bars show data binned by 45° , to enhance signal-to-noise ratio. The data in (*b*) are the subset of data in (*c*). The x -axis is position angle in the plane of the sky, increasing counterclockwise from north.

plot mean offset in every bin, along with the error of the mean. The data are displayed over two periods in position angle. As suggested by the figure, some azimuthal zones are displaced in distance (see, e.g., Fig. 13*b*), which supports our interpretation. In addition, moderately high values of reduced χ^2 (all of our plane fits in Table 4 have $\chi^2/\nu \sim 1.3$ or greater) also indicate problems with planar fits.

5.3. Comparison with MC01 Analysis

The results from our ring analysis in the previous section are in direct contradiction to the results of MC01, who state in their § 9.1 that their derived position angle θ is independent of the adopted LMC origin. Taken at face value, this suggests

that either (1) one of the analyses is wrong, or not sensitive enough, or (2) the two analyses are looking at a different structure, traced by different populations. Recall that our analysis is based on Cepheids, which are rather young (ages $\lesssim 300$ Myr), while MC01 analyze the distribution of carbon stars, which constitute the intermediate-age (~ 1 Gyr) population. We address each of the two possibilities in turn.

Comparing the relative accuracies of the two analyses, it is obvious that our analysis is significantly more accurate, for several reasons:

1. The analysis in MC01 is based on AGB (mostly carbon-rich) stars, which offer excellent sky coverage across the face of the LMC out to almost 7° from the center. The stars are

selected from DENIS and 2MASS data sets based on their colors. The analysis uses modal magnitudes of the luminosity function, which has approximately Gaussian peak with the width $\sigma = 0.3$ mag. (The width of the peak characterizes the quality of the standard candles.) The present study uses Cepheids, which are much better standard candles, with $\sigma = 0.13$ mag in the NIR, i.e., a factor of 2.5 improvement. All things being equal, this implies that the MC01 study needs at least 6 (2.5^2) times as many stars in R1 as we do to have the same accuracy. How do the numbers of stars in the two analyses compare? The number of Cepheids in R1 is approximately 550 (615 for H I center, 531 for MC01 center). MC01 do not say how many stars were in their first ring, but one may estimate it from the following: the total number of color-selected stars in their Figure 3 is 13,400. If we assume that carbon stars are in an exponential disk with the scale length $r_d = 1.44$ (van der Marel 2001) and further assume that the disk is truncated at 6.7 , we can estimate the fraction of stars in R1 as

$$\frac{\exp(-2.5/1.44)(1 + 2.5/1.44)}{1 - \exp(-6.7/1.44)(1 + 6.7/1.44)} - \frac{\exp(-3.4/1.44)(1 + 3.4/1.44)}{1 - \exp(-6.7/1.44)(1 + 6.7/1.44)} = 0.175.$$

(Note that the fraction is even lower if the disk is not truncated.) This means that in the first radial ring of MC01, there are $13,400 \times 0.175 \approx 2350$ stars. Note, however, that about a third of these stars are in the faint tail of the luminosity function as a result of red giant branch stars (see Fig. 3 of MC01). Thus, the number of stars in R1 that define the modal magnitude is $2350 \times \frac{2}{3} \approx 1600$, i.e., only a factor of ~ 3 more than in our R1. A similar result is obtained by direct count of 2MASS carbon stars with $1.5 < J - K_s < 2.0$, $K_s < 12.0$: there are 6374 stars in this region of the color-magnitude diagram. When the first ring cut is applied, it leaves 1000–1100 stars, depending on the choice of origin, i.e., only a factor of ~ 2 more than the number of Cepheids in R1. This is clearly less than needed for MC01 results to have the same accuracy as our Cepheid analysis. Note, however, that the difference in formal errors between MC01 and our analysis is too small to explain the 3σ ($\approx 30^\circ$) difference in position angles for H I centered at H I rotation center.

2. MC01 derive their results assuming that variations in magnitude are due to distance effect *only*. Our § 3.1 stipulates that variations in magnitude are due to distance and reddening variations (clearly a more accurate assumption, as suggested by LMC reddening maps). MC01 do address the effect of reddening on their results in their § 9.4 and conclude that “azimuthal variations in dust absorption do not affect the analysis at a significant level.” Apart from being essentially qualitative, the statement is flawed for two reasons. First, Figure 6 in MC01, which is used as evidence to show that the results are not affected by dust absorption, shows the results for all rings combined. In effect, MC01 compute radial averages for their sectors. Clearly, when one considers smaller data sets (concentric rings), the effect of reddening will be more pronounced, as local values of dust absorption may differ from mean LMC reddening quite significantly. Second, and more importantly, the MC01 argument that variations due to dust absorption are within the error bars in their Figure 6 and, hence, negligible is based on the implicit assumption that reddening variations are random with azimuth. With its pronounced azimuthal structure, the reddening may affect the data points in their Figure 6

systematically, i.e., shifting up all points for position angles in some range, and shifting them down for opposite points in the disk. This means that even if, as stated in MC01, the corrections due to reddening variations are within the error bars in their Figure 6, the systematic change may still affect the derived position angle significantly. It should be mentioned that the MC01 result for R1 centered at $(\alpha_0, \delta_0) = (82.25, -69.5)$ appears unaffected by these shortcomings, since they are in good agreement with our result for the same ring, probably because R1 with that center excludes high-reddening regions near 30 Dor. The MC01 assumption of uniform reddening may still bias their results for the H I rotation center. To conclude, regardless of whether arguments in § 9.4 of MC01 are correct or not, we emphasize that solving for distances and reddenings for individual stars, as done in our analysis, is better than solving for distances only and discussing the effect of reddening afterward, as done in MC01.

3. MC01 derive their results using four NIR magnitudes (I, J, H, K), while our analysis employs five-band photometry (V, R, J, H, K). In a simple interpretation, this one extra band should increase the figure-of-merit ratio of the two analyses by an extra factor of 1.25. However, in reality it is probably even more than that, since MC01 solve for disk orientation using data from one band at a time, while in our analysis we derive the results from all five bands simultaneously. Using multicolor photometry takes into account complex interplay among magnitudes and isolates the part of magnitude variations that is due to distance only (color independent) and anything else (age, metallicity, reddening, etc.).

The conclusion from this comparison is that *if* the two data sets do indeed trace the same populations in R1, then the results of this study are to be preferred over those in MC01, as more accurate. The question is then, do Cepheids and carbon stars trace the same structure? In particular, as implied by the results from R1, can we conclude that carbon stars in R1 are in the thin disk and Cepheids are not? Unfortunately, the answer to this question can only be provided by a detailed study of the carbon stars in the inner LMC, and such a study has not yet been done. Arguments can be made both for and against the conjecture. For example, one can claim that since Cepheids represent a younger population than carbon stars, their scale height in the disk should be smaller, and hence they should trace the disk better than carbon stars. On the other hand, while true for normal galaxies, this argument may not apply to an interacting system such as the LMC. Some of the Cepheids (in particular, the long-period ones) may still be associated with the H I gas from which they formed, and there is evidence that H I gas in the inner LMC is disturbed (Luks & Rohlfs 1992; Kim et al. 1998; Graff et al. 2000). Another argument can be made based on the bar populations: the LMC bar is prominent in sky distributions of both Cepheids (see Fig. 1) and carbon stars (van der Marel 2001), suggesting that both populations have the same spatial distribution near the LMC center. However, this argument is not conclusive, as the two populations can conceivably have different three-dimensional distributions while having similar disposition in the sky. To reiterate, the final answer should be derived from an in-depth analysis of carbon stars in the inner LMC.

Therefore, the issue is still open whether carbon stars and Cepheids in the inner LMC do trace the same structure. If they do indeed trace the same underlying structure, then MC01 results should depend on the adopted LMC center, and the fact that they do not means that the analysis in R1 is not sensitive enough to resolve structure made apparent by using better

standard candles and more sophisticated analysis. We stress that this possible problem with MC01 analysis applies only to radial zone R1, and to a lesser degree, to R2. The strength of the MC01 method is based on their considering stars far away from the LMC center, where planar geometry is usually not called into question. Thus, the MC01 results for two outer zones may still be correct, especially when combined with kinematic results from van der Marel et al. (2002), also driven by stars at large radii.

To summarize, most planar fits in the central LMC ($\rho \lesssim 4^\circ$) consistently give line-of-node position angle $\theta = 145^\circ - 150^\circ$. At large radii, the line of nodes twists to $\theta = 120^\circ - 130^\circ$, and LMC appears strongly elliptical, $\epsilon = 0.25 - 0.30$ (van der Marel 2001). The twist of the line of nodes from small to large radii indicates that the LMC is warped.

5.4. Is LMC Bar Aligned with the Plane?

Another issue that we can address is whether the bar of the LMC is misaligned with the main disk. With the persisting puzzle of the lensing population toward the LMC, it has been suggested (Zhao & Evans 2000) that the bar of the LMC may be misaligned with the disk or even displaced by a few kiloparsecs from the disk plane. Using our distance data, we can examine the relative distances of the bar and the disk. We define the bar as the rectangular region in our x_0 - y_0 plane, using the inequalities

$$\begin{aligned} y_0 &> 0.5x_0 - 0.8, \\ y_0 &< 0.5x_0, \\ y_0 &> -2x_0 - 5.3, \\ y_0 &< -2x_0 + 2.7. \end{aligned} \quad (14)$$

If a star's coordinates satisfy all inequalities given by equation (14), it is designated a "bar" Cepheid; otherwise, we consider it a "disk" star. Using the inequalities given by equation (14) gives 1509 disk Cepheids and 553 bar Cepheids. Once the disk and bar Cepheids are separated, we calculate a suitable projection to emphasize possible differences in distance between the disk and the bar. In this case, the best viewing angle is along the line of nodes. The coordinate transformation is a simple rotation about the z_0 axis clockwise, by $\pi - \theta$. The results are shown in Figure 14, where we plot both our selection of bar stars and the distance offsets for disk and bar Cepheids. The right-hand panel of Figure 14 has two interesting features:

1. The LMC disk, when viewed along the line of nodes, appears warped. The warp is symmetric, with an amplitude of $\lesssim 1$ kpc. The linear least-squares fit to the disk Cepheids is affected by the warp, which explains the moderately high reduced χ^2 from our disk models. The warp is also seen in the two-dimensional map of residuals (see § 5.5).

2. The bar of the LMC seems aligned with the disk plane but offset toward the Milky Way by a small distance. To calculate the offset between disk and bar, we model disk and bar data by linear regression separately (straight line fits are shown in the figure). The fits are

$$\begin{aligned} z' &= -0.614(0.035)x' - 0.205(0.056) \quad (\text{disk}), \\ z' &= -0.528(0.162)x' + 0.318(0.095) \quad (\text{bar}). \end{aligned}$$

While the slopes of the two lines are consistent with each other (disk and bar are aligned), the zero points are different

at a statistically significant level (3σ). Our analysis implies that the bar is offset from the main plane by ~ 0.5 kpc and is located in front of the disk. The end points of our bar in Figure 14 have smaller offsets due to probable mixing with disk stars, since our bar boundaries, denoted by the inequalities given by equation (14), are less well defined along the bar's major axis than along its minor axis (cf. Fig. 1). Obviously, for disk and bar separation based on sky coordinates, some disk contamination is expected across the entire "bar," which suggests that our estimate is a lower limit on the actual offset.

5.5. Residuals from Plane Fit

Figure 15 shows the distance residuals after the thin-disk fit (solution 3 in Table 4) has been subtracted. The two-dimensional map confirms both results conveyed by Figure 14: the bar in front of the disk and the symmetric warp. The map was obtained by binning the individual residuals and computing the variance-weighted average in each bin. The bins with less than four stars were set to zero, to reduce the noise. The resulting image has been smoothed with a circular Gaussian kernel, using $\sigma = 0.4$ kpc in each coordinate. Because of the smoothing, the numerical values for the warp amplitude and the bar offset read out from the plot are lower limits on actual values. The effect is in addition to the "smoothing" of the features by the plane fit itself.

A couple of points can be made in relation to Figure 15. First, a valid concern has to be addressed that these variations are not in fact real, but artifacts of the data. For example, correlations in photometric zero point ($\sigma = 0.1$ systematic photometric error in § 2.1) could mimic the distance variations in Figure 15, as a result of aperture corrections being similar for MACHO template fields observed on the same night. The effect will be somewhat reduced, since the distances are derived from five-band photometry (including NIR) and not MACHO data only. Nevertheless, to make sure this did not affect our results, we compared the observing dates for MACHO templates with the spatial positions of the offsets in Figure 15, on a field-by-field basis. No obvious correlation was detected, suggesting that the features in the figure are real.

Second, we address a possible effect of " $\Delta\mu - \Delta E(B-V)$ " correlation mentioned in § 4.2 on the residuals in Figure 15. As a result of the negative correlation between derived reddening and distances, there may be some concern that some of the variations in Figure 15 are induced by overestimated (underestimated) reddening for the corresponding location. We note, however, that the effect is strong only for individual Cepheids, not for statistical ensembles of stars. The averaging and smoothing procedure employed to produce the residual map ensures that the effect is small and the distance variations in Figure 15 are real.

6. SUMMARY

In this work we have analyzed five-band photometry of the more than 2000 LMC Cepheids, obtained from MACHO and 2MASS. Using MACHO light curves in V , R , we have corrected 2MASS observations for random phases. After deriving the best-fitting PL relations, we obtained the distance and reddening to each Cepheid from residuals to these relations. Our main results are the following:

1. New viewing angles for the LMC are derived. We find them a moderate function of adopted LMC center. For the H I

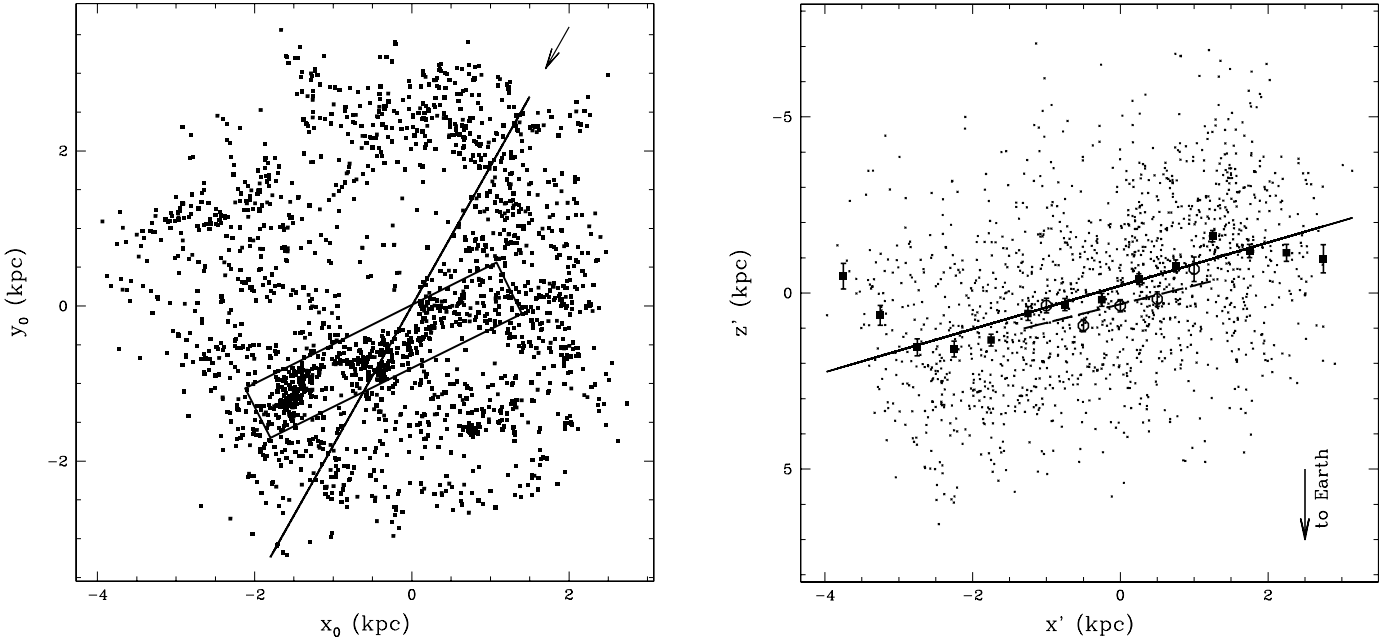


FIG. 14.—Analysis of spatial separation of LMC bar and disk. *Left:* Selection of bar Cepheids (*box*) and the adopted line of sight for coordinate transformation. The arrow indicates the line of sight for an imaginary observer, i.e., observer is in the sky plane looking along the line of nodes. *Right:* Distance offsets for all stars (*crosses*) and mean binned offsets for disk (*squares*) and bar (*circles*) Cepheids. The error bars indicate the errors of the binned means (i.e., weighted by number of stars per bin). Straight lines indicate linear least-squares fits to disk data (*solid line*) and bar data (*dashed line*). The offset between the two is ~ 0.5 kpc.

rotation center, we obtain $\theta = 151^\circ 0 \pm 2^\circ 4$, $i = 30^\circ 7 \pm 1^\circ 1$. The estimate is based on the inner LMC disk data, $\rho < 4^\circ$. These results support the typical LMC values previously obtained from a variety of tracers.

2. Analyses based on photometric data from concentric rings in the inner LMC are strongly dependent on the adopted

LMC center. Our calculations indicate that, depending on the coordinate origin in the inner disk, the results for viewing angles of the LMC can differ by as much as 35° . This result may reconcile the apparent spectrum of results for the LMC viewing angles available in the literature, in particular, the outlying value from MC01. We find that, using Cepheids from the first two radial rings, $2^\circ 5 < \rho < 3^\circ 4$ and $3^\circ 4 < \rho < 4^\circ 4$, by setting the LMC center to the MC01 value, we can reproduce their result for a low position angle.

3. A possible distance offset between disk and bar of the LMC is examined. After separating disk and bar based on sky coordinates, we find that the bar is aligned with the disk but displaced by ~ 0.5 kpc toward the observer. The offset bar is probably due to the dynamical interactions between the Milky Way, LMC, and SMC.

4. We find evidence for a symmetric warp in the LMC disk, seen in both the residual map and the projected distances. The amplitude of the distortion is ≥ 0.3 kpc (lower limit). The warp explains moderately high χ^2/dof values for planar disk fits, obtained from our analysis. Both the warp and the offset bar also explain the sensitivity of results derived from ring analysis to the adopted position of the LMC origin.

5. We find a number of Cepheids apparently far away (> 7 kpc) from the main disk. The stars are located both in front of (33 stars) and behind (11 stars) the main disk, with ~ 10 Cepheids in either location. These might be tracers of lensing population toward the LMC. We plan to examine them in a separate study.

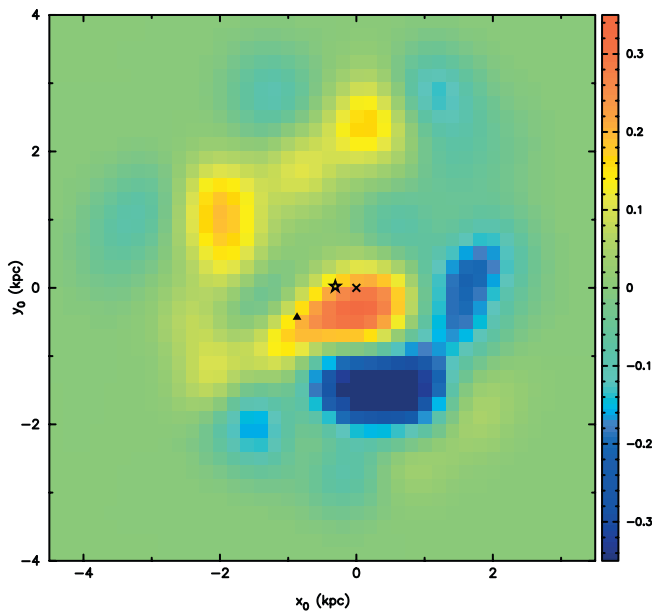


FIG. 15.—Map of residuals from planar solution. The map was obtained by binning residuals, computing variance-weighted average in each bin, and smoothing the resulting distribution with a Gaussian kernel ($\sigma_x = \sigma_y = 0.4$ kpc). To reduce the noise in the map, we only used bins with number of stars in them greater than 3. Negative (positive) residuals denote material behind (in front of) the fitted plane. The meaning of the symbols is the same as in Fig. 11.

This work was performed under the auspices of the US Department of Energy, National Nuclear Security Administration by the University of California, Lawrence Livermore National Laboratory under contract W7405-Eng-48. This publication

makes use of data products from the Two Micron All Sky Survey, which is a joint project of the University of Massachusetts and the Infrared Processing and Analysis Center, funded by the National Aeronautics and Space Administration and the National Science Foundation. N. D. acknowledges the

support of NASA through Hubble Fellowship grant HST-HF-01148.01-A awarded by STScI, which is operated by AURA for NASA, under contract NAS5-26555. The authors would like to thank the referee, Roeland van der Marel, whose detailed comments helped to improve the manuscript.

REFERENCES

- Alcock, C., et al. 1999, *PASP*, 111, 1539
 ———. 2000, *ApJ*, 542, 281
 Bessell, M. S., & Brett, J. M. 1988, *PASP*, 100, 1134
 Caldwell, J. A. R., & Coulson, I. M. 1985, *MNRAS*, 212, 879
 ———. 1986, *MNRAS*, 218, 223
 Cardelli, J. A., Clayton, G. C., & Mathis, J. S. 1989, *ApJ*, 345, 245
 Carpenter, J. M. 2001, *AJ*, 121, 2851
 Epchtein, N. 1998, in *IAU Symp. 179, New Horizons from Multi-Wavelength Sky Surveys*, ed. B. J. McLean, D. A. Golombek, J. J. E. Hayes, & H. E. Payne (Dordrecht: Kluwer), 106
 Freedman, W. L. 1988, *ApJ*, 326, 691
 Gibson, B. K., et al. 2000, *ApJ*, 529, 723
 Gochermann, J., Schmidt-Kaler, Th., & Oestreicher, M. O. 1992, in *New Aspects of Magellanic Cloud Research*, ed. B. Baschek, G. Klare, & J. Lequeux (Lecture Notes in Phys. 416; Heidelberg: Springer), 98
 Graff, D. S., Gould, A. P., Suntzeff, N. B., Schommer, R. A., & Hardy, E. 2000, *ApJ*, 540, 211
 Groenewegen, M. A. T. 2000, *A&A*, 363, 901
 Harris, J., & Zaritsky, D. 2001, *ApJS*, 136, 25
 Harris, J., Zaritsky, D., & Thompson, I. 1997, *AJ*, 114, 1933
 Keller, S. C., & Wood, P. R. 2002, *ApJ*, 578, 144
 Kim, S., Staveley-Smith, L., Dopita, M. A., Freeman, K. C., Sault, R. J., Kesteven, M. J., & McConnell, D. 1998, *ApJ*, 503, 674
 Labhardt, L., Sandage, A., & Tammann, G. A. 1997, *A&A*, 322, 751
 Laney, C. D., & Stobie, R. S. 1986, *MNRAS*, 222, 449
 Luks, Th., & Rohlfs, K. 1992, *A&A*, 263, 41
 Madore, B. F., et al. 1999, *ApJ*, 515, 29
 Martin, N., Prévot, L., Rebeiro, E., & Rousseau, J. 1976, *A&A*, 51, 31
 Massey, P. 2002, *ApJS*, 141, 81
 Ngeow, C.-C., Kanbur, S. M., Nikolaev, S., Tanvir, N. R., & Hendry, M. A. 2003, *ApJ*, 586, 959
 Nikolaev, S., Weinberg, M. D., Skrutskie, M. F., Cutri, R. M., Wheelock, S. L., Gizis, J. E., & Howard, E. M. 2000, *AJ*, 120, 3340
 Oestreicher, M. O., & Schmidt-Kaler, T. 1996, *A&AS*, 117, 303
 Olsen, K. A. G., & Salyk, C. 2002, *AJ*, 124, 2045
 Schwering, P. B. W. 1989, *A&AS*, 79, 105
 Skrutskie, M. 1998, in *The Impact of Near-Infrared Sky Surveys on Galactic and Extragalactic Astronomy*, ed. N. Epchtein (Dordrecht: Kluwer), 11
 Stetson, P. B. 1996, *PASP*, 108, 851
 Taylor, B. J. 1986, *ApJS*, 60, 577
 Udalski, A., Szymański, M., Kałużny, J., Kubiak, M., & Mateo, M. 1992, *Acta Astron.*, 42, 253
 Udalski, A., Szymański, M., Kubiak, M., Pietrzyński, G., Soszyński, I., Woźniak, P., & Żebruń, K. 1999, *Acta Astron.*, 49, 201
 van der Marel, R. P. 2001, *AJ*, 122, 1827
 van der Marel, R. P., Alves, D. R., Hardy, E., & Suntzeff, N. B. 2002, *AJ*, 124, 2639
 van der Marel, R. P., & Cioni, M.-R. L. 2001, *AJ*, 122, 1807 (MC01)
 Weinberg, M. D., & Nikolaev, S. 2001, *ApJ*, 548, 712
 Welch, D. L., McLaren, R. A., Madore, B. F., & McAlary, C. W. 1987, *ApJ*, 321, 162
 Westerlund, B. E. 1997, *The Magellanic Clouds* (Cambridge: Cambridge Univ. Press)
 Zaritsky, D. 1999, *AJ*, 118, 2824
 Zaritsky, D., Harris, J., & Thompson, I. 1997, *AJ*, 114, 1002
 Zhao, H.-S., & Evans, N. W. 2000, *ApJ*, 545, L35